The nucleus accumbens shell regulates hedonic feeding via a rostral hotspot

Alina-Măriuca Marinescu (1,*), Eshita Kamal (1), Peter Leary (2), Keila Navarro I Batista (3), Manuel Klug (1), Nataša Savić (4), Christelle Le Foll (3), Marie A. Labouesse (1,5,*)

1) Department of Health Sciences and Technology, ETH Zurich, Zurich, Switzerland;
2) Functional Genomics Center Zurich, University of Zurich/ETH Zurich, Zurich, Switzerland;
3) Institute of Veterinary Physiology, University of Zurich – Vetsuisse, Zurich, Switzerland;
4) ETH Phenomics Center, ETH Zurich, Zurich, Switzerland;
5) Neuroscience Center Zurich, University and ETH Zurich, Zurich, Switzerland

* Corresponding authors: alinamariuca.marinescu@hest.ethz.ch and marie.labouesse@hest.ethz.ch

KEY WORDS

anterior-posterior, aversion, consumption, fiber photometry, food intake, molecular diversity, neural circuits, neuroanatomy, nucleus accumbens, nucleus accumbens shell, optogenetics, reward, rostral-caudal, RNA sequencing, topographical gradients.

ABSTRACT

The medial nucleus accumbens shell (medNAcSh) is increasingly recognized as a key node in the regulation of hedonic feeding, exerting strong control over reward consumption through its projections to downstream structures. Recent studies showed that one of the primary cellular mediators of these effects are dopamine 1 receptor positive striatal projection neurons (D1-SPNs). Specifically, population D1-SPN activity gets inhibited during reward consumption and such inhibition is necessary and sufficient to authorize reward consumption, independent of metabolic need. Anatomically, the medNAcSh spans a 1.5 mm distance along the rostro-caudal axis in mice and previous studies have reported functional gradients along this axis in behavioral control. For instance, classical pharmacological studies have suggested that rostral rather than caudal medNAcSh regulates appetitive behavior. However, the cellular, circuit, and molecular mechanisms underlying this topographical gradient remain unknown. Here we hypothesized that D1-SPNs contribute to this gradient by regulating hedonic feeding via a specific hotspot in the rostral medNAcSh. Using population level calcium monitoring with fiber photometry in mice, we show that rostral medNAcSh D1-SPNs demonstrate inhibitory responses during reward consumption, while caudal D1-SPNs do not. Consistently, optogenetic stimulation of rostral medNAcSh D1-SPNs inhibits consumption, while stimulation of caudal D1-SPNs had minimal effects, confirming the existence of a functional rostro-caudal gradient. Importantly, we observed no differences between rostral and caudal D1-SPNs in their behavioral or activity responses to aversive stimuli, suggesting that the D1-SPN gradient is specific to appetitive contexts. To investigate potential molecular correlates of this functional gradient, we leveraged open-source anatomy datasets and performed fluorescent in situ hybridization, identifying Stard5 and Peg10 as markers enriched in the rostral and caudal medNAcSh, respectively. Finally, we developed a novel Stard5-Flp driver mouse line, which allowed us to target the rostral hotspot selectively. We demonstrated that Stard5+ neurons recapitulate activity patterns of rostral medNAcSh D1-SPNs. Together, these findings establish a spatially confined rostral subregion of the medNAcSh as a critical regulator of reward consumption and introduce Stard5 as a molecular tool for its manipulation - offering new opportunities for intervention in dysregulated eating beyond classical homeostatic circuits.

INTRODUCTION

Feeding behavior is a multifaceted physiological process governed by interconnected homeostatic and hedonic feeding brain circuits (Marinescu and Labouesse, 2024; Stuber et al., 2025; Zhu et al., 2025). While homeostatic pathways in the hypothalamus and brainstem regulate energy balance according to metabolic signals, non-homeostatic hedonic circuits are distributed more broadly throughout the brain to adjust feeding behavior according to sensory signals, motivation, associative learning or pleasure (Stuber et al., 2025). Among key brain regions involved in the latter, the nucleus accumbens shell (NAcSh) has emerged as a significant player, in particular its most medial section, the medial NAcSh (medNAcSh) (reviewed in (Marinescu and Labouesse, 2024)). Pharmacological studies in the 1990s and 2000s in rodents showed that inactivation of the medNAcSh dramatically increases the consumption of food rewards, even in fed animals (Maldonado-Irizarry et al., 1995; Stratford and Kelley, 1997). The medNAcSh consists of a mixed population of neurons of which a considerable proportion pause during reward consumption, an inhibitory signal that is necessary and sufficient to authorize food consumption, i.e. excitation suppresses, and pauses permit feeding (Domingues et al., 2025; Krause et al., 2010; O'Connor et al., 2015; Pedersen et al., 2022; Roitman et al., 2005; Taha and Fields, 2006, 2005). These pauses are driven primarily by cortical and limbic incoming circuits into the medNAcSh (Reed et al., 2018; Vachez et al., 2021), can be found in individual dopamine 1 receptor-positive striatal projection neurons (D1-SPNs) and D2-SPNs (Domingues et al., 2025; O'Connor et al., 2015; Pedersen et al., 2022), and are thought to allow rapid control over food consumption in response to motivational or sensory signals (Kelley et al., 2005; O'Connor et al., 2015). Importantly, recent studies showed that one of the primary cellular mediators of the eating-inhibitory effects in the medNAcSh are D1-SPNs, one of the two main output populations of the NAc (O'Connor et al., 2015; Thoeni et al., 2020; Bond et al., 2020).

Topographically, the NAcSh spans a 1.5 mm distance along the rostro-caudal (anterior-posterior) axis in mice with studies demonstrating strong polarity gradients along this axis in the control of various behaviors (Castro et al., 2016; Daniel C. Castro and Berridge, 2014; Krause et al., 2010; Reed et al., 2018; Reynolds and Berridge, 2008, 2002; Richard and Berridge, 2011). For instance, microinjection of the glutamate antagonist DNQX or the GABA agonist muscimol into the rostral medNAcSh promotes appetitive responses like feeding, while the same manipulations in the caudal medNAcSh triggers aversive behaviors (Reynolds and Berridge, 2001; Richard and Berridge, 2011). D1, but not D2 antagonists were able to block the glutamate-mediated feeding responses in the rostral medNAcSh, suggesting a more important role for the D1-SPN pathway (Richard and Berridge, 2011). Altogether, these findings suggest the existence of a hotspot for feeding located in the rostral sections of the medNAcSh possibly involving D1-SPNs. However, the cellular, circuit, and molecular mechanisms underlying this rostral hotspot remain unknown.

Against this background, we hypothesized that D1-SPNs regulate feeding behavior according to a rostro-caudal gradient within the medNAcSh. We use fiber photometry recordings and optogenetic activation studies, finding a functional dichotomy between rostral vs. caudal medNAcSh D1-SPNs in reward consumption but not in aversive behavioral assays. We perform neuroanatomical investigations in the rostral vs. caudal medNAcSh and identify various circuit and molecular signatures of these two subregions, including a molecular marker, Stard5, densely expressed in 80% of rostral medNAcSh D1-SPNs and D2-SPNs. Finally, we generate a new Flp driver line which targets the Stard5 rostral medNAcSh subpopulation and use it in proof of concept experiments, finding that Stard5 cells replicate the population-level activity signatures of rostral medNAcSh D1-SPNs during reward consumption and aversion. Our work outlines the importance of functional and molecular gradients in the medNAcSh, demonstrating the existence of a D1 rostral hotspot for feeding in the medNAcSh that is partly recapitulated by Stard5+ cells, a newly described molecular marker to access this feeding hub. These findings

offer new potential access points for targeting dysregulated eating through a spatially confined medNAcSh region, outside traditional homeostatic feeding circuits.

RESULTS

Rostral medNAcSh D1-SPNs regulates feeding

We first set to identify points of divergence in the feeding-related properties of D1-SPNs along the rostro-caudal medNAcSh axis. It is well established that, although D1-SPNs show both excitatory and inhibitory responses during feeding, a considerable proportion of cells are inhibited, in the form of prolonged pauses (Domingues et al., 2025; Krause et al., 2010; O'Connor et al., 2015; Pedersen et al., 2022; Roitman et al., 2005; Taha and Fields, 2006, 2005) which can be reflected at population level activity (Domingues et al., 2025). These pauses are thought to authorize eating by disinhibiting downstream circuits (O'Connor et al., 2015; Thoeni et al., 2020; Bond et al., 2020). To determine whether such pause responses change along the rostro-caudal axis, we used fiber photometry to measure population level D1-SPN activity in both the rostral and caudal medNAcSh while sated mice were fed a palatable food source (condensed milk). Drd1-cre mice received an adeno-associated virus (AAV) expressing a cre-dependent calcium indicator (jGCaMP8m (Y. Zhang et al., 2023)) and an optic fiber above the rostral or caudal medNAcSh, targeting specifically the dorsal region given its strong role in feeding (O'Connor et al., 2015) (**Figure 1a-b;** see also **Supplementary Figure S1**). Mice were allowed to consume up to 30 food rewards per session delivered at random intervals (**Figure 1c**). As expected, population D1-SPN activity in the rostral medNAcSh showed a prolonged pause upon reward consumption, with average activity decreasing at eating onset, and returning to baseline after the 10 s consumption period (**Figure 1d**). This was reflected by a significant decrease in the ΔF/F0 minima during the consumption as compared to pre-consumption period (**Figure 1e**). The inhibition of D1-SPN activity during reward consumption in rostral medNAcSh aligns well with previous findings (Krause et al., 2010; O'Conner et al., 2015, Thoeni et al., 2020; Bond et al., 2020). On the other hand, D1-SPNs in the caudal medNAcSh showed an acute excitatory response at consumption onset that returned to baseline after ~2.5 s, followed by a minor prolonged inhibition (**Figure 1f**). This was reflected by a significant increase in the ΔF/F0 maxima in the consumption as compared to pre-consumption period (**Figure 1g**). These data indicate a strong divergence in the responses of D1-SPNs to reward consumption depending on their topographical location, highlighting the existence of a rostro-caudal gradient. It further demonstrates that the rostral, but not caudal, medNAcSh represents the primary locus for the expression of pause responses by D1-SPNs at a population level during reward consumption.

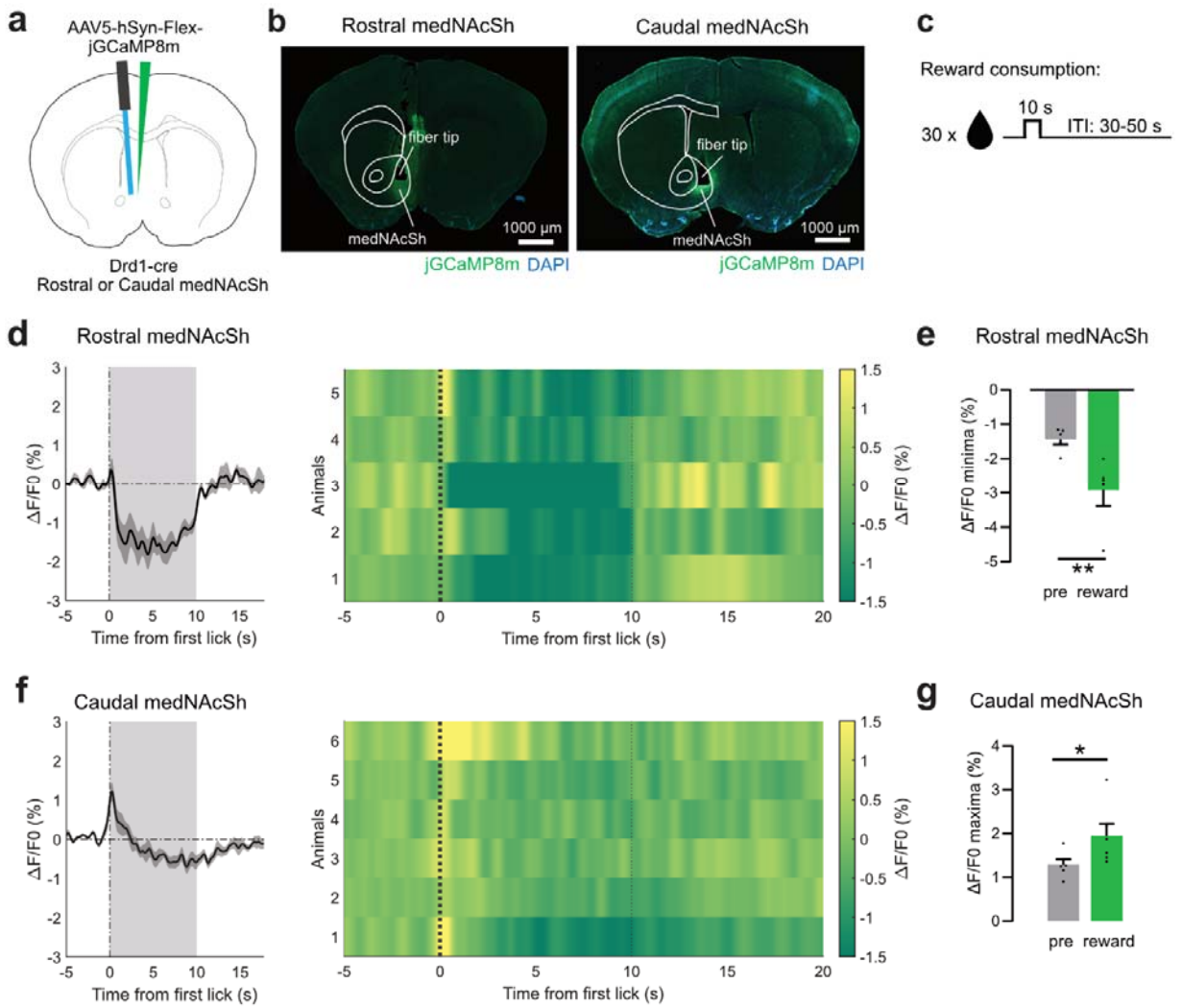

Fig 1. D1-SPNs in the rostral vs. caudal medNAcSh respond differentially to reward consumption. a. Surgery schematics of Drd1-cre mice injected with a cre-dependent calcium indicator (jGCaMP8m) and implanted with unilateral optic fibers in the rostral or caudal medNAcSh to image calcium photometry signals. **b.** Representative coronal images of rostral (left) vs. caudal (right) medNAcSh mice. **c.** Protocol for the unpredicted reward consumption behavioral task: 30 rewards were available for 10 s at random intervals. **d.** Left: Average calcium activity in D1-SPNs (all trials) shown as normalized fluorescence (ΔF/F0, %) in the rostral medNAcSh over time aligned to the onset of reward consumption, i.e. first lick onset (0 s). Grey shading represents the 10 s epoch for reward consumption. Right: Heatmap showing average calcium activity across individual trials (each row represents an animal) aligned to reward consumption i.e. lick onset (0 s, thick dotted line). Thin dotted line: end of reward access. **e.** Quantification of the data in (d.) depicts a significant decrease in rostral medNAcSh activity upon reward consumption, as shown by a significant decrease in ΔF/F0 minima in the 0 to 5 s reward epoch vs. -6 to -1 s pre-reward epoch. Paired t-test, $t(4) = 4.610$, $p = 0.0100$. N = 5 mice. **f.** same as (d.) for the caudal medNAcSh. **g.** Quantification of the data in (f.) depicts a significant increase in caudal medNAcSh activity upon reward consumption, as shown by a significant increase in ΔF/F0 maxima in the 0 to 5 s reward epoch vs. -6 to -1s pre-reward epoch. Paired t-test, $t(5) = 3.059$, $p = 0.0281$. N = 6 mice. Data is mean ± SEM. *p<0.05; **p<0.01; ***p<0.001. See also **Supplementary Figure S1**.

Previous work showed that medNAcSh D1-SPNs can also causally impact hedonic eating, where optogenetic activation of D1-SPNs (using rostral-centric medNAcSh coordinates) inhibits reward consumption while optogenetic inhibition promotes consumption independent of metabolic needs (Bond et al., 2020; O'Connor et al., 2015). This is similar to what is found with global, cell-unspecific, medNAcSh pharmacological inhibition (Maldonado-Irizarry et al., 1995; Stratford and Kelley, 1997). Based on this extensive literature and our photometry results, we asked whether reward consumption effects were confined to the rostral side of the medNAcSh or whether similar functions extended to the caudal medNAcSh. Drd1-cre mice received bilateral injections of an AAV expressing a cre-dependent excitatory opsin, ChrimsonR, and optic fibers above the rostral or caudal medNAcSh (**Figure 2a-b**). We first conducted a proof-of-concept experiment in a small cohort to validate previously published optogenetic protocols. Mice were exposed to palatable food rewards with alternating blocks of 8 min: blocks 1 and 3 without laser stimulation (laser off) and block 2 with stimulation (laser on) (**Figure 2c**). In ChrimsonR Rostral medNAcSh mice, lick count was initially high with laser off, then decreased during laser on, and rebounded again with laser off. This consumption pattern is very similar to what is seen in the literature (Bond et al., 2020; O'Connor et al., 2015). When averaging lick counts per epoch type, we could detect a significant reduction in reward consumption with optogenetic stimulation of rostral medNAcSh D1-SPNs. No significant change in consumption was seen in mCherry controls. Although these mice began with a slightly lower (non-significant) baseline compared to ChrimsonR mice, there was no evidence of a floor effect (**Figure 2d-e**). Altogether, this feasibility experiment confirmed published findings (Bond et al., 2020; O'Connor et al., 2015), namely that activation of rostral medNAcSh D1-SPNs inhibit reward consumption. We then went on to test a full experimental cohort to evaluate the differential contribution of rostral vs. caudal medNAcSh D1-SPNs in reward consumption. Here we modified the protocol to enhance the sensitivity of the assay, minimize potential confounds such as increasing satiety over time and improve our ability to detect even minor differences in reward consumption between the three groups. We started with a laser on epoch and expanded the number of epochs from 3 to 5 (3 laser on, 2 laser off); we also reduced epoch duration from 8 to 5 min (**Figure 2f**). As before, and despite the modified protocol, we again found that optogenetic stimulation of D1-SPNs in the rostral medNAcSh significantly inhibited reward consumption with no effects in mCherry controls (**Figure 2g-i**). A similar (as seen in **Figure 2d**) rebound in consumption was detected after laser on epochs in rostral medNAcSh mice but not mCherry controls (**Figure 2g**). Importantly, although there was a non-significant trend for an opto-mediated eating-inhibitory effect in caudal medNAcSh mice (see **Figure 2g**), and the number of caudal medNAcSh animals demonstrating opto-mediated inhibition of consumption was 64% (vs. 100% of rostral medNAcSh mice and 30% mCherry) (**Figure 2i**), the mean effect was too small to reach statistical significance ($p = 0.5244$) (**Figure 2h**). In sum, rostral, but not caudal, medNAcSh D1-SPNs inhibit reward consumption. Altogether this indicates the existence of a rostro-caudal gradient in the regulation of hedonic eating by medNAcSh D1-SPNs, supporting the existence of a D1 rostral medNAcSh appetitive hotspot.

Rostral and caudal medNAcSh D1-SPNs show similar function in aversive assays

Previous work has shown that the medNAcSh plays strong roles in not only appetitive but also aversive behaviors (Al-Hasani et al., 2015; de Jong et al., 2019; Domingues et al., 2025; Liu et al., 2022; Yang et al., 2018; Zhou et al., 2022). For instance, Liu et al. showed that medNAcSh D1 projections to the ventral pallidum (VP) (but not the ventral tegmental area, VTA) are acutely activated by aversive stimuli and in turn optogenetic stimulation of these projections promotes aversion in a real time place preference vs. avoidance assay (RTTPA) (Liu et al., 2022). We therefore asked whether regulation of aversive behaviors by medNAcSh D1-SPNs differed along the rostro-caudal axis, as was the case for the reward consumption task (**Figure 1,2**). Using fiber photometry, we first recorded D1-SPN population activity in the rostral and caudal medNAcSh while mice were exposed to aversive

stimuli in the form of 10 unpredicted shocks delivered at random intervals (**Figure 3a-b**). We found that both rostral and caudal D1-SPNs showed similar responses (albeit not fully overlapping in the period post-shock), with both groups depicting strong acute excitatory responses to the shocks (**Figure 3c,e**). This was reflected by a significant increase in the ΔF/F0 in the shock vs. pre-shock period in both groups (**Figure 3d,f**). We then tested the impact of optogenetic stimulation of these same neurons in a well established RTPPA assay (Al-Hasani et al., 2015; Liu et al., 2022; Zhou et al., 2022) (**Figure 3g-i**). We found that optogenetic stimulation of both rostral and caudal medNAcSh D1-SPNs promoted avoidance of the opto-paired chamber, with no effects in controls, suggesting that stimulation of these neurons is aversive. These data indicate that medNAcSh D1-SPNs generally promote aversion without major differences along the rostro-caudal axis. This lack of functional differences between the two subregions contrasts with other studies showing divergent activity patterns or functional responses in the same photometry or RTTPA assays when comparing medial to lateral NAcSh (Chen et al., 2023) or medNAcSh D1-SPN projections to different downstream regions (Liu et al., 2022). Altogether our data highlight the existence of a rostral D1 medNAcSh hotspot that is primarily restricted to an appetitive feeding context.

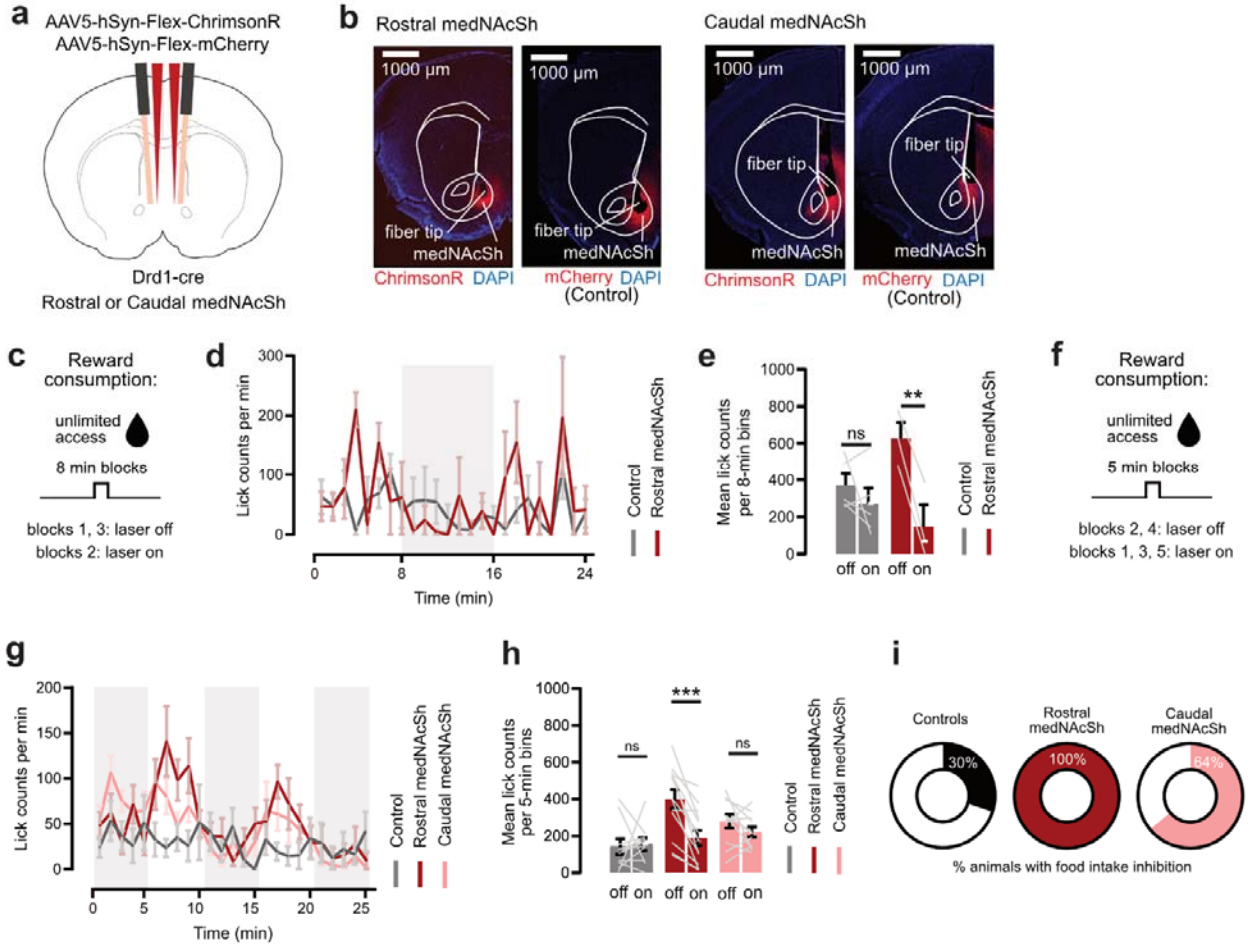

Fig 2. In vivo optogenetic stimulation of rostral medNAcSh inhibits reward consumption. a. Surgery schematics of Drd1-cre mice injected with a cre-dependent activating opsin (ChrimsonR) or mCherry control AAV and implanted with bilateral optic fibers in the rostral or caudal medNAcSh to stimulate local D1-SPNs. **b.** Representative coronal images of rostral (left) vs. caudal (right) medNAcSh mice expressing relevant AAVs. **c.** Protocol for the proof-of-concept reward consumption experiment: mice had unlimited access to the reward spout.

Blocks of 8 min without (laser off, ‘non-opto’) or with opto-stimulation (laser on, ‘opto’) were alternated (off/on/off) for a total of 3 blocks. **d.** Quantification of the lick counts per min in mCherry mice vs. ChrimsonR (rostral medNAcSh) mice, showing a lower lick count per min in rostral medNAcSh mice during opto stimulation vs. ‘non-opto’ epochs; lick counts unchanged across epochs in mCherry mice. **e.** Quantification of mean licks per session in the opto-stimulation vs. non-opto-stimulation epochs shows a significant decrease in lick counts following stimulation of rostral medNAcSh D1-SPNs (and not in mCherry controls) confirming published studies. 2-way RM-ANOVA (group x epoch). Main effects: group $F(1,6) = 0.4089$, $p = 0.5461$; epoch $F(1,6) = 18.44$, $p = 0.0051$; group x epoch $F(1,6) = 7.846$, $p = 0.0311$. Sidak post-hoc opto-stimulation vs. non opto-stimulation: Controls $t(6) = 1.219$, $p = 0.4648$; ChrimsonR Rostral medNAcSh $t(6) = 4.488$, $p = 0.0083$; N = 5 Controls; N = 3 ChrimsonR Rostral medNAcSh. **f.** Protocol for the full reward consumption experiment: mice had unlimited access to the reward spout. Blocks of 5 min with or without opto-stimulation were alternated (on/off/on/off/on) for a total of 5 blocks. **g.** Quantification of the lick counts per min, showing that ChrimsonR rostral medNAcSh mice eat less during on vs. off epochs as in **d.**; there is a trend for a similar observation for ChrimsonR caudal medNAcSh mice. No change across epochs for mCherry control mice, as in (**d.**). **h.** Quantification of mean licks per session in the opto-stimulation vs. non-opto-stimulation epochs shows a significant decrease in lick counts following stimulation of rostral, but not caudal medNAcSh D1-SPNs (and no change in mCherry controls) indicating that activation of rostral but not caudal medNAcSh D1-SPNs significantly decrease reward consumption. 2-way RM-ANOVA (group x epoch). Main effects: group $F(2,31) = 4.548$, $p = 0.0185$; epoch $F(1,31) = 10.58$, $p = 0.0028$; group x epoch $F(2,31) = 6.651$, $p = 0.0039$. Sidak post-hoc opto-stimulation vs. non opto-stimulation: Controls $t(31) = 0.2669$, $p = 0.9909$; Rostral medNAcSh $t(31) = 5.010$, $p < 0.0001$; Caudal medNAcSh $t(31) = 1.253$, $p = 0.5244$. N = 10 Controls; N = 13 Rostral medNAcSh; N = 11 Caudal medNAcSh. **i.** Pie charts showing % of mice showing food intake inhibition (mean Δlick counts non-opto/opto>0) in each group: 100% of ChrimsonR rostral medNAcSh mice, 30% of controls; and although caudal medNAcSh opto-stimulation does not lead to significant reward consumption inhibition as shown in **h.**, 64% of mice show an inhibition, indicating the effect is present but the effect size is too small to get captured statistically. Data is mean ± SEM. *p<0.05; **p<0.01; ***p<0.001. See also **Supplementary Figure S1**.

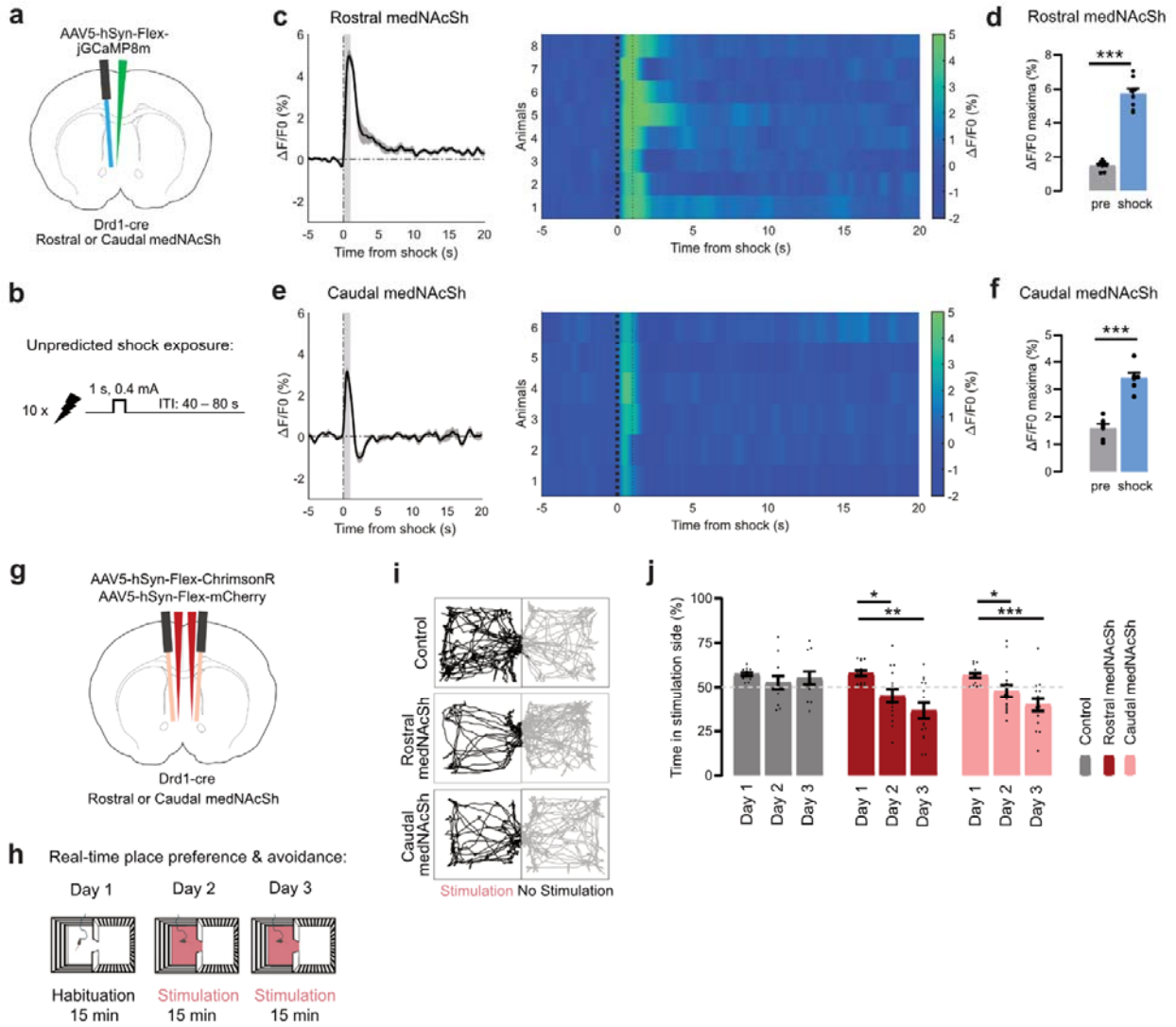

Fig 3. D1-SPNs in the rostral vs. caudal medNAcSh respond similarly to aversion. a. Surgery schematics of Drd1-cre mice injected with a cre-dependent calcium indicator (jGCaMP8m) and implanted with unilateral optic fibers in the rostral or caudal medNAcSh to image calcium photometry signals. **b.** Protocol for the unpredicted shock behavioral task: 10 shocks (0.4 mA) were available for 1 s at random intervals. **c.** Left: Average calcium activity in D1-SPNs (all trials) shown as normalized fluorescence (ΔF/F0, %) in the rostral medNAcSh over time aligned to shock onset (0 s), showing acute excitation at shock onset, followed by a slow return to baseline. Grey shading: shock epoch. Right: Heatmap showing calcium activity across individual trials (each row represents a trial) aligned to shock onset (0 s, thick dotted line). Thin dotted line: end of shock. **d.** Quantification of the data in (**c.**) depicts a significant increase in rostral medNAcSh activity upon shock onset, as shown by a significant increase in ΔF/F0 maxima in the 0 to 5 s shock epoch vs. -6 to -1s pre-shock epoch. Paired t-test, $t(7) = 14.91$, $p = 0.0001$. N = 8 mice. **e.** same as (**d.**) for the caudal medNAcSh showing acute excitation at shock onset, followed by a rapid return below zero before returning to baseline; the significance of this is unknown. **f.** same as (**d.**) for the caudal medNAcSh. Paired t-test, $t(5) = 8.312$, $p = 0.0004$. N = 6 mice. **g.** Surgery schematics of Drd1-cre mice injected with a cre-dependent activating opsin (ChrimsonR) or mCherry control AAV and implanted with bilateral optic fibers in the rostral or caudal medNAcSh to stimulate local D1-SPNs. **h**. Protocol for the real-time place preference or avoidance (RTPPA) behavioral task: After 1 habituation (unstimulated) day, mice were tested on 2 days where opto-stimulation occurred as soon as mice entered the laser-paired chamber (session duration 15 min). **i.** Representative locomotor patterns of animals in the RTPPA chamber on day 3 in all groups. **j.**

Quantification of the percent (%) time spent in the stimulation side vs. non-stimulated side. Opto-stimulation led to a decrease in the time spent in the stimulation chamber in rostral medNAcSh and caudal medNAcSh mice but not in mCherry mice, indicating that activation of rostral and caudal medNAcSh D1-SPNs is aversive. 2-way RM-ANOVA (group x day). Main effects: group $F(2,39) = 3.539$, $p = 0.0387$; day $F(1.822,71.05) = 19.08$, $p = 0.0001$; group x day $F(4,78) = 3.302$, $p = 0.0149$. Sidak post-hoc day 2 vs. day 1: Controls $t(11) = 1.232$, $p = 0.4277$; Rostral medNAcSh $t(14) = 2.951$, $p = 0.0209$; Caudal medNAcSh $t(14) = 2.700$, $p = 0.0342$. Sidak post-hoc day 3 vs. day 1: Controls $t(11) = 0.5776$, $p = 0.8195$; Rostral medNAcSh $t(14) = 4.250$, $p = 0.0016$; Caudal medNAcSh $t(14) = 4.661$, $p = 0.0007$. N = 12 Controls; N = 15 Rostral medNAcSh; N = 15 Caudal medNAcSh. Data is mean ± SEM. ns non-significant; *p<0.05; **p<0.01; ***p<0.001. See also **Supplementary Figure S1**.

Molecular rostro-caudal gradients across the medNAcSh highlight Stard5 and Peg10 as unique markers

Rostro-caudal functional differences in feeding could reflect distinct molecular compositions across the medNAcSh. Indeed, recent work using fluorescent in-situ hybridization (FISH) or single-cell RNA sequencing (scRNAseq) has delineated the strong molecular and spatial diversity within the NAc (Chen et al., 2021; Stanley et al., 2020), identifying cellular clusters within D1-SPNs and/or D2-SPNs that express combinations of marker genes and are often enriched in spatial subregions of the NAc. Hence it is possible that unique molecular markers are enriched in the rostral vs. caudal medNAcSh and contribute to functional differences. We used published in-situ hybridization datasets from the Allen Mouse Brain Atlas to identify novel molecular markers enriched in one of these two subregions. Screening 48 markers flagged by the Allen Brain Atlas as expressing in the NAc, we found that most genes showed relatively stable expression across the rostro-caudal axis (e.g. Rasal1, LOC381076, Stra6, Lypd1; which are representative examples shown in **Supplementary Figure S2**). However, we detected 5 genes depicting differential rostro-caudal gradient expression: Stard5, Smug1 and Cartpt were enriched in the rostral medNAcSh while Peg10 and Sgsm1 were enriched in the caudal medNAcSh (**Figure 4a**), which was also confirmed by optical density analysis (**Figure 4b**). Among all markers, Stard5 and Peg10 showed particular strong enrichment in the rostral and caudal medNAcSh, respectively, as opposed to neighboring regions (**Figure 4b**). These data demonstrate the existence of molecular gradients across the rostro-caudal axis of the medNAcSh and highlight Stard5 and Peg10 as markers enriched in rostral vs. caudal medNAcSh, respectively.

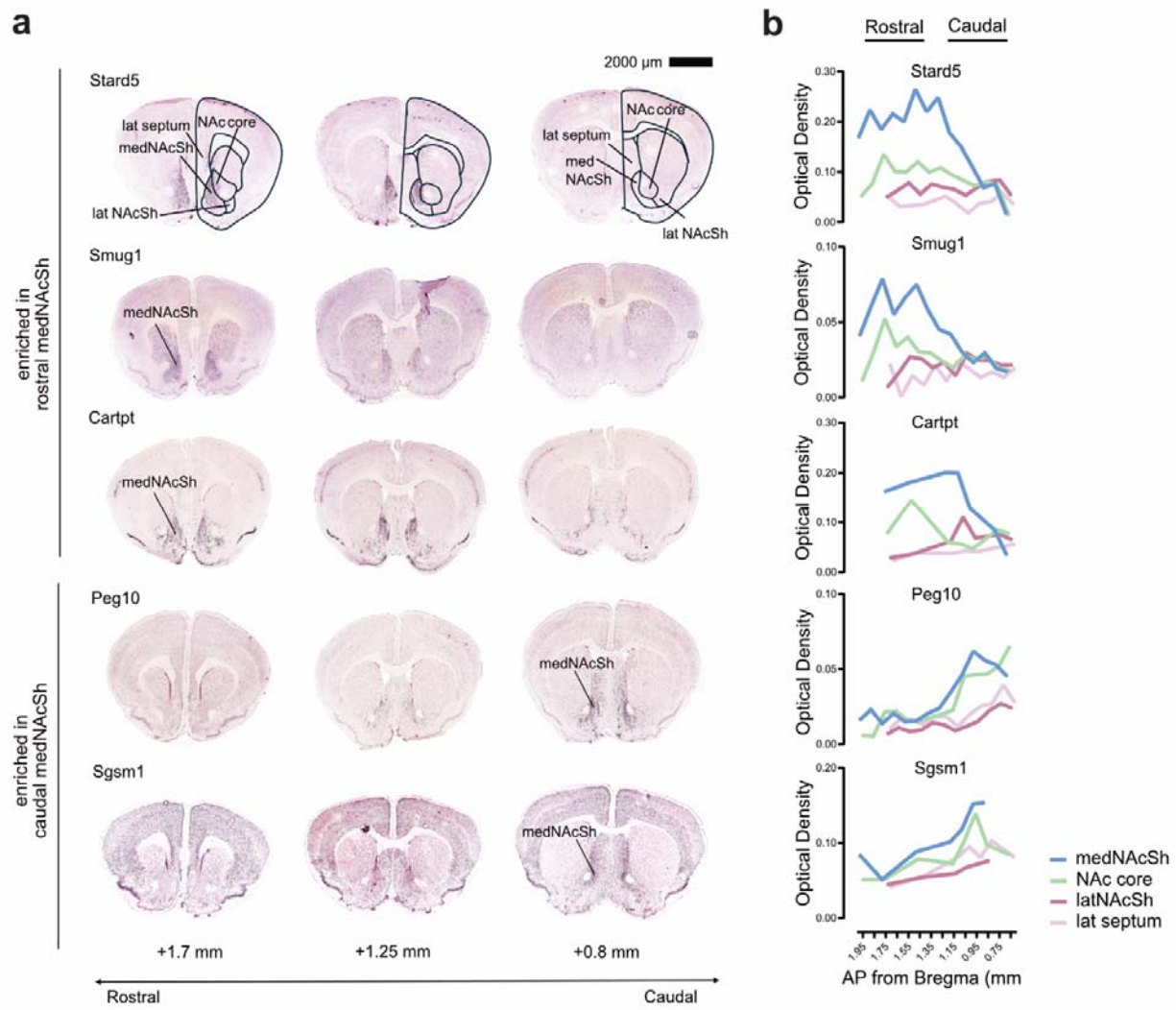

Fig 4. Stard5 is enriched in the rostral region and Peg10 in the caudal region of the medNAcSh, respectively. a. Representative in-situ hybridization images obtained from the Allen Brain Atlas (https://mouse.brain-map.org/) for 5 markers showing enriched expression in the rostral medNAcSh (Stard5, Smug1, Cartpt) or the caudal medNAcSh (Peg10, Sgsm1). Data for the NAc core, lateral NAcSh (latNAcSh) and lateral septum (lat septum) are also shown. All 48 markers available in the Allen Brain Atlas labeling the nucleus accumbens were screened. Images on the left are more rostral (bregma +1.65 mm); images on the right are more caudal (bregma +0.85 mm). **b.** Quantification of expression levels of markers from a. in the medNAcSh along the rostral-caudal axis (bregma +1.95 mm to +0.75 mm) using optical density measurements (n = 1 mouse, 7-14 sections total, data shown is the mean from 2 measures/section). Stard5, Smug1 and Cartpt show enrichment in the rostral medNAcSh with Stard5 showing the strongest total expression and strongest relative expression in medNAcSh as compared to other regions. Peg10 and Sgsm1 show enrichment in the caudal medNAcSh with Peg10 showing the strongest relative expression in medNAcSh as compared to latNAcSh and lateral (lat) septum (but not NAc core). See also **Supplementary Figure S2**.

We analyzed a published scRNAseq dataset of the entire NAc (core and shell) (Chen et al., 2021) to further characterize the cellular expression patterns of Stard5 and Peg10 (**Figure 5a-c**, see also below). We found that, in the NAc, Stard5 is expressed predominantly in D1-SPNs (34.91% of Stard5+ cells) and D2-SPNs (30.41%) with lesser expression in other cell types, mostly interneurons (17,60%) (**Supplementary Figure S3a**).

A similar pattern was observed for Peg10 with strongest expression in D1-SPNs (36.52% of Peg10+ cells), D2-SPNs (26.69%) and interneurons (33.13%) (**Supplementary Figure S3b**).

Since Stard5 and Peg10 are expressed in both D1- and D2-SPNs, we performed triple FISH to further characterize their expression profiles within these two main cell populations (D1- and D2-SPNs) across subregions of the NAc (**Figure 5d,f**). First, we confirmed that Stard5 is strongly expressed within the D1-SPN (30.62% of Drd1+ cells) and D2-SPN (32.47% of Drd2+ cells) populations amongst the entire NAc, similar to what we see with scRNAseq 'entire NAc' data (29.55% of Drd1+ cells and 38.19% of Drd2+ cells) (**Figure 5b**). Importantly, subregion analyses revealed that Stard5 is predominantly expressed in the rostral and intermediate sections of the medNAcSh, in particular its dorsal part, precisely the rostral feeding hotspot identified in this study and others (Reed et al., 2018; Reynolds and Berridge, 2001; Richard and Berridge, 2011) (**Figure 5e**). Stard5 was expressed in a large majority of D1-SPNs (79% of Drd1+ cells) and D2-SPNs (76% of Drd2+ cells) in the dorsal rostral medNAcSh (**Figure 5e**), hence representing an almost ubiquitous marker for SPNs in this region. Stard5 expression in D1-SPNs and D2-SPNs gradually decreased when moving more caudally, ventrally and laterally into the NAc core and lateral shell (**Figure 5e**), confirming that its expression follows a molecular gradient rather than a binary on/off expression. We performed the same FISH analysis for Peg10, and found a similar gradient pattern with strongest expression in the caudal medNAcSh and gradually decreasing expression moving more rostrally, ventrally and laterally (**Figure 5f,g**). In the caudal medNAcSh, Peg10 was expressed in 16.45% of D1-SPNs (Drd1+) and 13.34% of D2-SPNs (Drd2+), similar to what we see with scRNAseq 'entire NAc' data (16.72% of Drd1+ cells and 16.09% of Drd2+ cells) (**Figure 5c**). Moreover, in caudal sections, Peg10 was enriched in dorsal and ventral medNAcSh D1-SPNs (33% dorsal and 31% ventral, of Drd1+ cells) similar to Stard5; while it showed relatively stable expression across NAc subregions for D2-SPNs (i.e. no medNAcSh enrichment) (**Figure 5g**). In summary, we confirm the existence of molecular gradients across the rostro-caudal medNAcSh axis, revealing Stard5 as a strong marker for both types of SPNs in the rostral medNAcSh feeding hotspot, in particular its dorsal part.

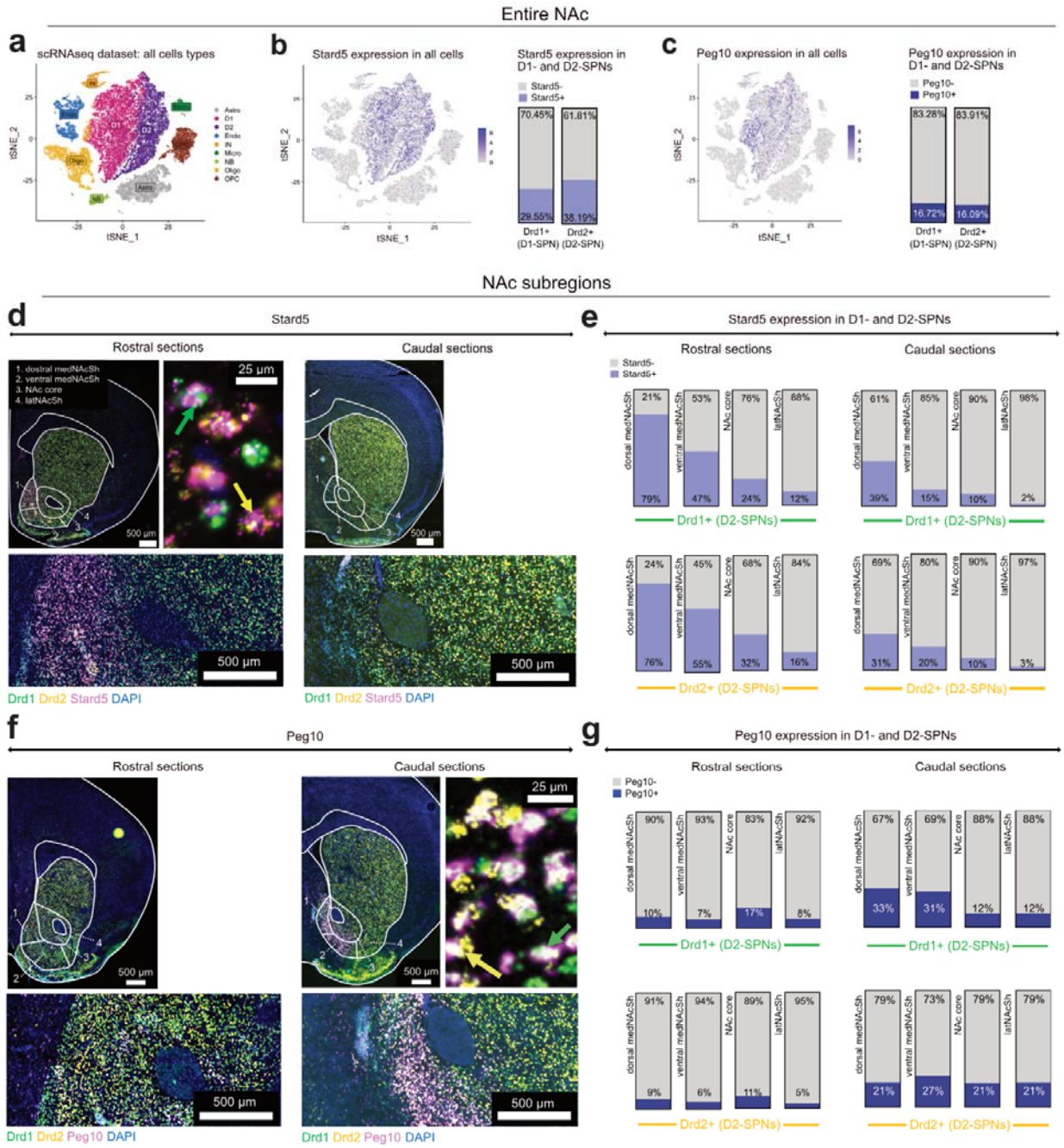

Fig 5. Stard5 is enriched in D1- and D2-SPNs of the rostral medNAcSh. a. t-SNE plot showing cell types in the entire NAc based on re-analysis of a published scRNAseq dataset, GSE118020 (Chen et al., 2021). Data is pooled from 11 mice, 36670 cells. Different cell clusters are color-coded. Clusters mark cell types identified by canonical markers, as used in (Chen et al., 2021). Astro: astrocytes, D1: D1-SPN, D2: D2-SPN, Endo: endothelial cells, IN: interneurons, Micro: microglia, NB: neuroblasts, Oligo: oligodendrocytes, OPC: oligodendrocyte progenitor cells. **b.** Left: t-SNE plots showing expression of Stard5 across NAc cells; the densest expression is found in the D1- and D2-SPNs clusters. Stard5 expression level is color-coded from 0 (low) to 6 (high). Right: Quantification of cells positive or negative for Stard5 within D1- and D2-SPNs (identified by Drd1 and Drd2 expression). About 1/3 of D1- and 1/3 of D2-SPNs express Stard5. **c.** Left: t-SNE plots showing expression of Peg10 across NAc cells; the densest expression is found in the D1-SPN, D2-SPN and interneuron clusters. Peg10 expression level is color-coded from 0 (low) to 6 (high). Right: Quantification of cells positive or negative for Peg10 within D1- and D2-SPNs (identified by Drd1 and Drd2 expression). A small proportion (16 to 17%) of

D1- and of D2-SPNs express Peg10. **d.** Left: Representative image of a fluorescent in-situ hybridization (RNAscope) assay for Drd1, Drd2 (labelling D1- and D2-SPNs) and Stard5 in subregions of the rostral and caudal sections of the NAc (dorsal and ventral medNAcSh, NAc core and latNAcSh). Lower panel: zoom-in and Right panel: high resolution magnification showing Stard5+,Drd1+ (green arrow) or Stard5+,Drd2+ (yellow arrow) neurons. **e.** Quantification of expression of Stard5 in D1- and D2-SPNs in subsections of the NAc (dorsal and ventral medial [med] NAcSh, NAc core and lateral [lat] NAcSh) in the rostral and caudal regions of the NAc. An average of 6-8 sections in total, including 2-3 for most rostral sections and 2-3 for most caudal sections; and 5 mice in total were analyzed. Data shows strong enrichment (75-80%) of Stard5 in D1- and D2-SPNs of the rostral, dorsal medNAcSh (and much less in the caudal medNAcSh or other NAc regions). See also **Supplementary Figure S3** showing minor Stard5 expression in other cell types. **f.** Same as (d.) for Peg10. **g.** Same as (e.) for Peg10 (n= 5 mice). Data shows enrichment of Peg10 in D1- and D2-SPNs of the dorsal and ventral caudal medNAcSh (very little expression in the rostral medNAcSh). See also **Supplementary Figure S3** showing Peg10 expression in interneurons (in addition to D1- and D2-SPNs).

Medial NAcSh Stard5 cells recapitulate phenotypes of rostral medNAcSh D1-SPNs

Stard5 could represent an interesting molecular marker to label or functionally target cellular populations in the rostral medNAcSh feeding hotspot. To evaluate this possibility, we used CRISPR/Cas9 genetic engineering to generate a new driver line, Stard5-Flp, expressing the Flp recombinase in Stard5+ cells (**Figure 6a, Supplementary Figure S4**), i.e. primarily in Stard5+ D1-SPNSs, D2-SPNs and interneurons. Stard5-Flp-positive mice bred well, were viable and showed no behavioral or metabolic abnormalities as compared to Stard5-Flp-negative mice indicating absence of obvious genomic off-target expression (**Supplementary Figure S5**). Stard5-Flp mice were injected with an AAV expressing a Flp-dependent fluorophore (jGCaMP8m) into the rostral medNAcSh or in neighboring regions (**Figure 6b**). We found strong fluorophore expression in the rostral medNAcSh but very low or no expression when injecting in the neighboring NAc core and dorsal striatum, respectively (**Figure 6c**), confirming that Stard5 expression is enriched in the medNAcSh as opposed to neighboring regions (**Figure 5**). Very low ectopic expression was found in Stard5-Flp negative mice (a ratio 1:16 vs Stard5-Flp positive mice, **Figure 6c**), confirming minimal (but not entirely absent) Flp leakage of the AAV construct, a very common yet often ignored issue, which could be mitigated in the future using modern AAV design strategies (Fischer et al., 2019).

Finally, we used the Stard5-Flp mouse to determine whether Stard5 cells recapitulate some of the feeding-related phenotypes of rostral medNAcSh D1-SPNs. Stard5-Flp mice were injected in the rostral medNAcSh with an AAV expressing a synaptophysin tagged Flp-dependent EGFP to evaluate the projection sites of rostral medNAcSh Stard5+ cells. We found strong expression in the VP, VTA and lateral hypothalamus (LH) (**Supplementary Figure S6**), confirming that Stard5+ cells project to the three classical projection targets of medNAcSh D1-SPNs (see **Supplementary Figure S1**) and D2-SPNs. Stard5-Flp mice were then injected with an AAV expressing a Flp-dependent calcium indicator (jGCaMP8m) and optic fibers implanted above the rostral medNAcSh to record the population activity of Stard5+ cells (**Figure 6d,e**). Similarly to rostral medNAcSh D1-SPNs, we found that Stard5+ cells pause during reward consumption (**Figure 6f-h**), and get acutely excited upon exposure to aversive stimuli (**Figure 6f,i-j**). This confirms that Stard5+ cells recapitulate some of the behavioral phenotypes of rostral medNAcSh D1-SPNs. It further suggests that Stard5 is a molecular marker of the rostral medNAcSh feeding hotspot.

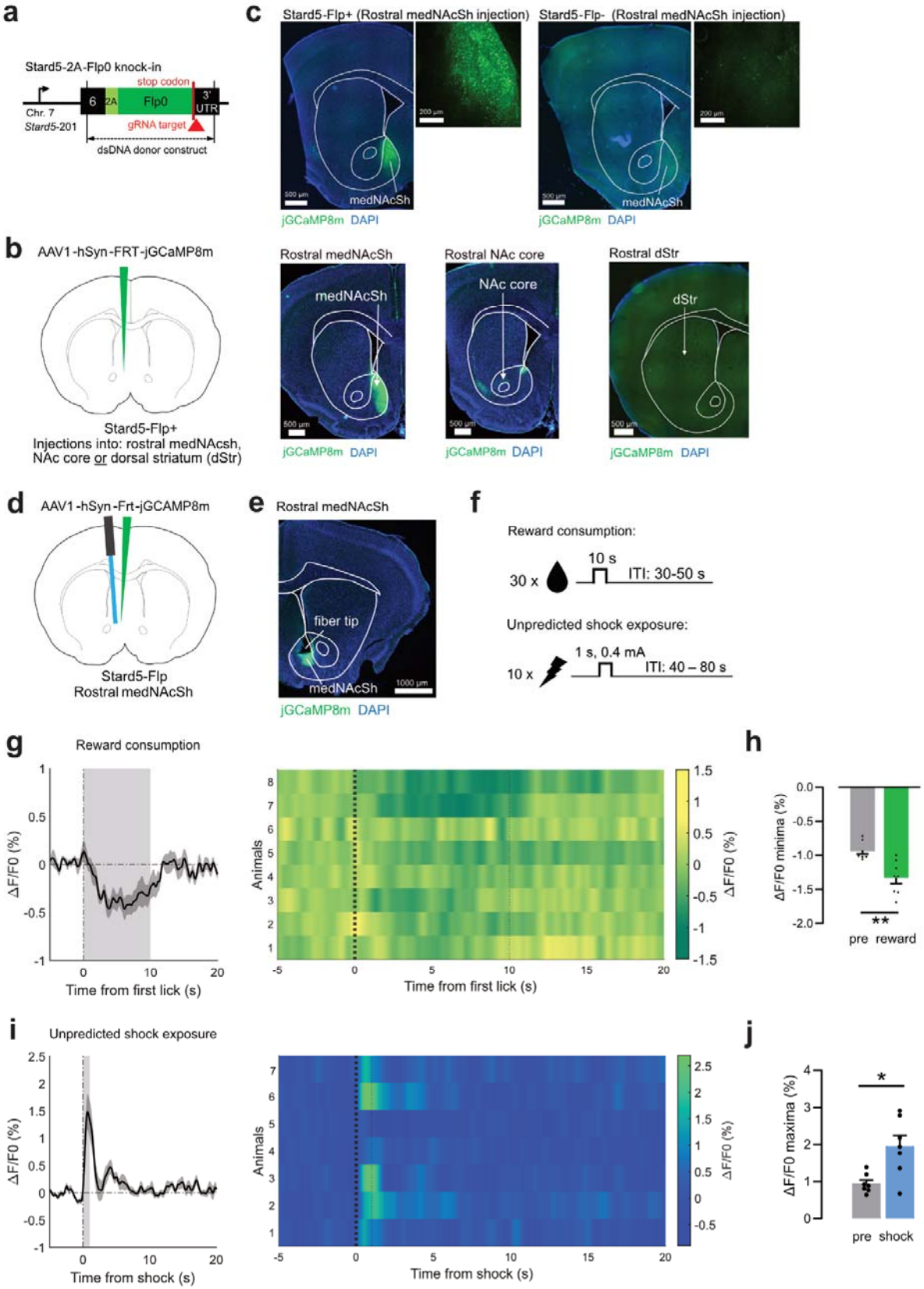

Fig 6. Stard5 is a molecular marker for the rostral medNAcSh feeding hotspot. a. CRISPR/Cas9-based strategy to generate a Stard5-2A-Flp0 knock-in mouse (abbreviated Stard5-Flp). A double-stranded (ds) DNA knock-in template expressing the Flp0 recombinase (dark green bands), the RAKR and T2A self-cleaving peptide (light green bands) and Stard5 homology arms spanning exon 6 and the 3'UTR of the Stard5 gene (black bands) was used to create the model. The guide (g)RNA (red triangle) targets the stop codon (blue) of the Stard5 gene

(Chromosome 7) at its most expressed transcript in the NAc (Stard5-201; see **Supplementary Figure S4**). Knock-in was achieved by homologous recombination. **b.** Left: Surgery schematic for the validation of the Stard5-Flp mouse. An AAV expressing a flp-dependent vector (jGCaMP8m) was injected into the rostral or caudal medNAcSh, dorsal striatum or NAc core of Stard5-Flp mice. **c**. Top: Representative coronal images and zoom-in showing successful expression of a Flp-dependent fluorophore in the rostral medNAchSh of Stard5-Flp mice, with very minimal expression in Stard5-Flp negative mice (few cells) indicating a minor Flp leak of the AAV. Close to no expression could be detected in the caudal medNAcSh, NAc core or dorsal striatum (dStr) after injection directly into those regions, confirming that, within the striatal complex, Stard5 expression is primarily confined to the medNAcSh. **d.** Surgery schematics of Stard5-Flp mice injected with a flp-dependent calcium indicator (FRT-jGCaMP8m) and implanted with unilateral optic fibers in the rostral medNAcSh to image calcium photometry signals. **e.** Representative coronal image of rostral medNAcSh Stard5-Flp mice expressing FRT-jGCaMP8m and implanted with an optic fiber. **f.** Top: Protocol for the unpredicted reward behavioral task: 30 rewards were available for 10 s at random intervals. Bottom: Protocol for the unpredicted shock behavioral task: 10 shocks (0.4 mA) were available for 1 s at random intervals. **g.** Left: Average calcium activity in Stard5+ neurons (all trials) shown as normalized fluorescence (ΔF/F0, %) in the rostral medNAcSh over time aligned to the onset of reward consumption, i.e. first lick onset (0 s). Grey shading represents the ~10 s epoch for reward consumption. Right: Heatmap showing calcium activity across individual trials (each row represents an animal) aligned to reward consumption. Thin dotted line: end of reward access. **h.** Quantification of the data in (g.) depicts a significant decrease in rostral medNAcSh Stard5 cell activity upon reward consumption, as shown by a significant decrease in ΔF/F0 minima in the 0 to 5 s reward epoch vs. -6 to -1 s pre-reward epoch. Paired t-test, $t(7) = 4.630$, $p = 0.0024$. N = 8 mice. **i.** Left: Average calcium activity in Stard5+ neurons (all trials) shown as normalized fluorescence (ΔF/F0, %) in the rostral medNAcSh over time aligned to shock onset (0 s). Grey shading: shock epoch. Right: Heatmap showing calcium activity across individual trials (each row represents a trial) aligned to shock onset. Thin dotted line: end of reward access. **j.** Quantification of the data in (i.) depicts a significant increase in rostral medNAcSh Stard5 cell activity upon shock exposure, as shown by a significant increase in ΔF/F0 maxima in the 0 to 5 s shock epoch vs. -6 to -1 s pre-shock epoch. Paired t-test, $t(6) = 3.305$, $p = 0.0163$. N = 7 mice. Data is mean ± SEM. *p<0.05; **p<0.01; ***p<0.001. See also **Supplementary Figures S4, S5, S6**.

DISCUSSION

In recent years the medNAcSh has gained increasing appreciation as a key brain region that controls hedonic feeding (reviewed in (Marinescu and Labouesse, 2024). At the cellular level, studies have shown that D1-SPNs, are one of the primary cellular mediators of these effects as they can rapidly and powerfully regulate the amount of food consumed in rodents independent of metabolic need (O'Connor et al., 2015; Thoeni et al., 2020; Bond et al., 2020; Maldonado-Irizarry et al., 1995; Stratford and Kelley, 1997). At the topographical level, in situ pharmacological studies have indicated the existence of a rostro-caudal gradient in the medNAcSh suggesting that its rostral but not caudal subregion is the primary hotspot for feeding regulation (Castro et al., 2016; Daniel C. Castro and Berridge, 2014; Krause et al., 2010; Reed et al., 2018; Reynolds and Berridge, 2008, 2002; Richard and Berridge, 2011). However, the cellular, circuit and molecular mechanisms of this gradient were, this far, unclear. Here, we combined fiber photometry, optogenetic and neuroanatomical experiments, identifying a strong functional dichotomy between rostral and caudal medNAcSh D1-SPNs in feeding behavior, but not in aversive assays, thus demonstrating the existence of a rostral medNAcSh D1-SPN feeding hotspot. Using open-source ISH and scRNAseq datasets and in-house FISH experiments, we show that functional gradients in the medNAcSh are paralleled by molecular gradients along the rostro-caudal axis, delineating the existence of Stard5

and Peg10 as markers of the rostral and caudal medNAcSh, respectively. Finally, we use our newly developed Stard5-Flp driver mouse line, finding that Stard5 cells replicate functional phenotypes of the rostral D1 feeding hotspot. This work provides insights into the functional and molecular organization of the medNAcSh in the context of feeding behavior and delineate a novel marker, Stard5, to access the rostral medNAcSh feeding hub.

Our work extends previous research delineating a behavioral and anatomical dichotomy between rostral and caudal sections of the medNAcSh (Baumgartner et al., 2020; Castro et al., 2016; Daniel C. Castro and Berridge, 2014; Faure et al., 2010; Krause et al., 2010; Pedersen et al., 2022; Reed et al., 2018; Reynolds and Berridge, 2008, 2002; Richard and Berridge, 2011) and align with similar concepts demonstrated in the dorsal striatum (Hintiryan et al., 2016; Valjent and Gangarossa, 2021). In our photometry work, we show that, at the population level, rostral medNAcSh D1-SPNs pause, while caudal medNAcSh are acutely excited upon reward consumption. This finding corroborates past work showing that forebrain excitatory inputs into the medNAcSh pause during consumption at rostral but not caudal medNAcSh sites (Reed et al., 2018) and that individual D1-SPN and D2-SPNs show rostro-caudal gradients in their responses to feeding (Pedersen et al., 2022). We also find that optogenetic stimulation of D1-SPNs in the rostral medNAcSh suppress reward consumption, while there was a trend for an eating-inhibitory effect that was not significant in the caudal medNAcSh, suggesting the existence of a gradient rather than a binary on/off phenomenon. This aligns with previous studies finding that in situ infusion of the glutamate antagonist DNQX or the GABA agonist muscimol in the rostral medNAcSh promotes appetitive responses like feeding, and the DNQX effects are suppressed by a D1 but not D2 antagonist (Reynolds and Berridge, 2001; Richard and Berridge, 2011). Interestingly, studies also found that DNQX or muscimol infusions into the caudal, but not rostral, medNAcSh promote aversive behaviors indicating the existence of rostro-caudal gradient also for aversion (Reynolds and Berridge, 2001; Richard and Berridge, 2011). Here in contrast we did not detect differences in aversive behaviors according to the rostro-caudal medNAcSh site, i.e. both rostral and caudal medNAcSh D1-SPNs showed excitation upon exposure to aversive stimuli and optogenetic stimulation of both cell types promoted avoidance in a RTPPA assay. This lack of divergent responses contrasts with published work identifying differences in either the photometry activity patterns or the RTTPA functional responses when comparing medial to lateral NAcSh (Chen et al., 2023) or medNAcSh D1-SPN projections to VP vs. VTA (Liu et al., 2022). In our study, the lack of differences could be due to the fact that our injection sites in rostral and caudal medNAcSh were too close to each other to to distinguish region-specific effects. However, since we did detect significant differences between rostral and caudal medNAcSh in the reward consumption photometry and optogenetic assays, this suggests that injection site proximity was not a limiting factor. Future studies using minimal AAV injection volumes and/or tapered optic fibers (Pisanello et al., 2017) would help to more precisely restrict the manipulation, thereby enabling refined dissection of spatially confined subregions. Another interesting possibility is that D2-SPNs mediate such rostro-caudal aversive gradient, a cell type we did not manipulate in the present study. This possibility would align with previous work showing that the modulation of aversive behaviors by the caudal medNAcSh requires both D1Rs and D2Rs (Richard and Berridge, 2011). Intriguingly, past studies found that rostro-caudal gradients are plastic, i.e. they can be retuned by the valence of the environment. While in a standard test chamber, rostral DNQX promotes feeding and caudal DNQX promotes aversion, the feeding zone expands caudally in a calm, home-like condition, while the aversion zone expands rostrally in a highly stressful condition (Baumgartner et al., 2020; Reynolds and Berridge, 2008; Richard et al., 2013; Richard and Berridge, 2011). Future work could address whether the same environmental retuning impacts the behavioral effects of medNAcSh D1-SPNs, and in turn what are the possible molecular or circuit mediators of these effects. Moreover, it would be interesting to determine if the food consumption effects of D1-SPN optogenetic manipulation are related to the avoidance effects in the RTPPA assay, i.e. is the inhibition of food consumption due to an internal

state of aversion. Since we show that optogenetic stimulation of the caudal medNAcSh induces aversion without suppressing food consumption, this suggests that aversive signaling and feeding behavior can be dissociated. Instead, our findings support the idea that D1-SPNs in the rostral medNAcSh function as a neural hub at the intersection of reward processing and motor (consumption) output. Future studies should dissect this further.

We here determined the projection patterns of medNAcSh subregions and find that the rostral and caudal medNAcSh both project to the LH (**Supplementary Figure S1**), an important feeding center (Rossi, 2023). Although in this study we did not quantify the density of projections, previous data identified a stronger medNAcSh to LH projection arising from rostral as compared to caudal medNAcSh sections (Thoeni et al., 2020). Such differential projections to the LH could explain behavioral differences between these two brain subregions as multiple studies have demonstrated a dominant role for the medNAcSh to LH projection in the D1-SPN eating effects (O'Connor et al., 2015; Stratford and Kelley, 1999; Thoeni et al., 2020). Since both LH GABA and LH glutamate neurons receive D1-SPN input (Liu et al., 2024; O'Connor et al., 2015; Thoeni et al., 2020; Zhou et al., 2022), future studies could investigate the relative contribution of these two cell types in the feeding effects of rostral medNAcSh D1-SPNs. The contribution of rostral medNAcSh D1-SPN projections to the VP and VTA (Bond et al., 2020; Pedersen et al., 2022) should also be addressed in future work. Moreover, whether D2-SPNs also regulate behavior differentially according to a rostro-caudal axis remains to be determined. Optogenetic activation of D2-SPNs in the medNAcSh did not affect feeding (O'Connor et al., 2015), but it is possible that rostro-caudal differences emerge when restricting manipulations to either subregion. Moreover, a recent preprint indicated that medNAcSh D2-SPNs, in particular its projections to the VP, regulate reward preference (Pedersen et al., 2022), while other studies have shown that the medNAcSh regulates not only food consumption but also food liking, food wanting (D.C. Castro and Berridge, 2014) and extinction in a Pavlovian task (Domingues et al., 2025). Hence the potential role of rostral and caudal medNAcSh D1- and D2-SPNs in food-related behaviors beyond the act of consumption could be addressed in future work.

Other possible circuit mechanisms could explain the rostro-caudal functional differences identified here, in particular the differential circuit inputs into the rostral vs. caudal medNAcSh. It is well established that the medNAcSh receives strong excitatory input from the ventral hippocampus (vHipp), amygdala (Amy), paraventricular nucleus of the thalamus (PVT) and prefrontal cortex (PFC) (reviewed in (Marinescu and Labouesse, 2024)). Interestingly, previous work found that these forebrain regions innervate the rostral and caudal medNAcSh via distinct cellular subpopulations (Reed et al., 2018). vHipp inputs to the rostral medNAcSh were also found to be stronger as compared to the caudal medNAcSh (Trouche et al., 2019). Moreover, optogenetic inhibition of excitatory inputs into the rostral medNAcSh promotes feeding, while similar phenotypes are not detected in the caudal medNAcSh (Reed et al., 2018). Hence it is very likely that differential innervation patterns into the rostral vs. caudal medNAcSh explain the emergence of a rostral feeding hotspot. Previous work demonstrated that, in addition to excitatory forebrain inputs, the VP also sends strong inhibitory inputs into the medNAcSh and directly regulates feeding (Vachez et al., 2021); future work could address the rostro-caudal innervation patterns of these VP arkypallidal cells and their contributions to functional differences.

Importantly, our work further suggests that differences in the molecular composition of the rostral vs. caudal medNAcSh could explain behavioral differences between these brain subregions. Indeed, we detected multiple markers showing enriched expression in the rostral vs. caudal medNAcSh. In particular, we identified and later validated Stard5 as a molecular marker labeling the rostral medNAcSh and Peg10 the caudal medNAcSh. Future work using spatial transcriptomics could extend these findings to identify further relevant rostro-caudal markers at the transcriptome-wide level (Piwecka et al., 2023). Importantly, we find that molecular markers do not exhibit a binary on/off expression pattern but rather demonstrate a gradient like pattern, being enriched vs. depleted in

specific subregions of the NAc. This aligns with previous scRNAseq and MERFISH studies highlighting the existence of spatial gradients of molecularly defined cells within the NAc or dorsal striatum (Chen et al., 2021; Stanley et al., 2020; M. Zhang et al., 2023). Authors outlined the existence of two types of markers: 1) cluster markers that selectively mark rare and unique cellular subtypes and 2) spatial markers that are broadly expressed in a spatially restricted manner within NAc subregions. One example of the former are Serpinb2 and Tac2, which labeled small and separate clusters of D1-SPNs in the medial NAc (Chen et al., 2021) and regulate behavior in a non-canonical manner (Liu et al., 2024; Zhao et al., 2022). Here we build on past findings (Chen et al., 2021; Stanley et al., 2020), showing that Stard5 is one of the latter, namely a spatial marker for a spatially defined subterritory, the dorsal part of the rostral medNAcSh. Rather than labeling a unique rare cell type, Stard5 expression is almost ubiquitous within D1- and D2-SPNs in that subregion (up to 80% of SPNs), making it a noteworthy marker to broadly target the projections of this functionally unique NAc subregion, the rostral medNAcSh feeding hotspot. Using our new Stard5-Flp mouse driver line, we confirm that rostral medNAcSh Stard5 cells recapitulate feeding-related phenotypes of rostral but not caudal medNAcSh D1-SPNs, confirming that molecular markers and spatial location intersect to define cellular function. One important caveat of the Stard5-Flp mouse is that it targets not only D1-SPNs but also D2-SPNs as well as other cell types (primarily interneurons) in the rostral medNAcSh. However, the Stard5-Flp line was designed using a Flp recombinase so that it could be crossed with selected cre lines to label more restricted cell types. This strategy could be used in future work to dissect the contribution of D1+ vs. non-D1+ Stard5 cells in the phenotypes we describe herein.

Together with multiple other studies (Chen et al., 2023; Liu et al., 2024; Zhao et al., 2022), our findings suggest that the molecular composition of NAc cellular clusters or NAc subregions strongly dictate their function. This aligns with recent work showing that other cellular properties such as spatial location, circuit inputs or circuit outputs also regulate function (Al-Hasani et al., 2015; Chen et al., 2023; Liu et al., 2024; Zhao et al., 2022; Zhou et al., 2022). For instance, recent work finds that medNAcSh cells receiving PVT input drive aversion via LH GABA neurons, while those receiving BLA input drive reinforcement via VTA GABA and LH glutamate cells (Zhou et al., 2022). Thus, the NAcSh is composed of intermingled neural circuits that can dictate behavioral outcome via multiple and sometimes opposing sub-circuits. The finding that NAc molecular composition strongly regulates function represents an important piece of information with critical implications for future therapeutic strategies. Indeed, if druggable targets such as receptors, transporters or enzymes can be identified as molecular markers labeling unique NAc subregions or unique NAc cell clusters, this could allow to develop targeted therapies to increase or decrease reward consumption in a specific manner by up or downregulating the activity of unique NAc cells.

Our study has potential applications in applied and therapeutic research. First, it could inform future studies investigating the neuronal regulation of body weight and energy balance by the NAc. In this study we show that the rostral medNAcSh acutely regulates food intake: it would be interesting to determine if these effects are persistent over several days and in turn if chronic modulation is sufficient to trigger changes in body weight or body composition. Although these experiments have not been conducted, previous work showed that synaptic plasticity at medNAcSh D1-SPN terminals in the LH regulates overeating over more than 24 hours (Thoeni et al., 2020). Moreover, we and others have used broader manipulations of the NAc or dorsal striatum showing that these brain regions as a whole can powerfully impact body weight, energy metabolism and obesity risk (Labouesse et al., 2018; Matikainen-Ankney et al., 2023; Walle et al., 2024). Hence, future work could determine whether the rostral medNAcSh plays particularly important roles in these effects. In addition, the NAc is implicated not only in food intake regulation but also in neuropsychiatric diseases like depression or addiction (Lüscher and Janak, 2021). Dissecting which subregions of the NAc regulates which types of behavior could have important

implications for the understanding of the pathophysiology of these brain disorders. For instance it would be interesting to determine whether the addiction-related impact of NAcSh D1-SPNs or incoming inputs also follow a rostro-caudal gradient (Corre et al., 2018; Gibson et al., 2018). The NAc is the target of multiple therapeutic agents including anti-depressants (Xu et al., 2020) or anti-obesity drugs, including glucagon-like peptide 1 (GLP-1) mimetics (Adan, 2013; Müller et al., 2022). Better delineating the cellular targets of these compounds could support the further refinement of these therapeutic agents into drugs with lesser side effects or stronger impact, e.g. by inhibiting hedonic eating to support weight loss or weight maintenance in the context of obesity. Although there are GLP-1 receptors in the NAc (shell and core), peripheral GLP-1 mimetics do not reach these brain regions due to limited blood-brain-barrier permeability (reviewed in (Marinescu and Labouesse, 2024)). Since the medNAcSh can get activated by GLP-1 agonists, (see e.g. (Labouesse et al., 2012)) these effects are likely occurring via indirect circuit effects. Moreover, the NAc is an important candidate for deep brain stimulation (DBS) treatment, in particular for obsessive compulsive disorder or depression (Bewernick et al., 2010; Creed et al., 2015; Nho et al., 2024) but also disorders of dysregulated eating (Hounchonou et al., 2023; Shivacharan et al., 2022; Zhang et al., 2015). Describing a topographical map of how NAc subregions controls various types of behavior could support the refinement of electrode targeting strategies in the context of DBS-based therapy.

In summary, our study provides clues into the cellular, circuit and molecular mediators of a rostro-caudal feeding gradient, identifying a D1 rostral hotspot in the medNAcSh with critical roles in feeding behavior. We describe a molecular marker, Stard5, that allows labeling the rostral medNAcSh feeding hotspot using a new Flp driver line. Our work also provides insights into the functional organization of the medNAcSh, demonstrating the importance of functional and molecular gradients. This could inform more localized targeting of future therapeutic interventions aiming at treating disorders of dysregulated eating.

METHODS

Mice

Adult (>8 weeks old) male and female C57Bl6/J mice, Drd1-cre (B6.FVB(Cg)-Tg(Drd1-cre)EY262Gsat/Mmucd) and Stard5-2A-Flp0 (C57BL/6J-Stard5(2A-FLPo)Em1Ethz/Mlab) (Stard5-Flp, generated for this paper; see below) backcrossed onto C57BL/6□J background were used for experiments. All animals were housed at 22-25˚C under a reversed 12-hour light-dark cycle (dark 8 am to 8 pm) fed with a regular chow diet (18.5% proteins, 4.5% fat, 4.5% fibers, 54.2% digestible carbohydrates; 3.85 kcal/g gross energy, #3437, Kliba-Nafag, Switzerland). Behavioral testing was done in the dark phase unless otherwise indicated. Animals for behavior were handled and if necessary habituated to patch cord tethering before testing. All animal procedures were performed in accordance to the Animal Welfare Ordinance (TSchV 455.1) of the Swiss Federal Food Safety and Veterinary Office and were approved by the Zurich Cantonal Veterinary Office or other relevant National and Institutional regulatory bodies.

Generation of the Stard5-2A-Flp-mice via Crispr/Cas9 genetic engineering

Analysis of Stard5 transcript expression in the striatum. We set out to design a Stard5-2A-Flp0 mouse line by inserting a 2A-Flp0 sequence to the 3'UTR of the Stard5 gene (prior to the stop codon). The Stard5 gene has 2 differential splicing variants that contain open reading frames (protein coding): Stard5-201 and Stard-202 which have different 3'UTR regions and terminal exons. To ensure 2A-Flp0 is targeted to a variant that is expressed in the NAc, we analyzed a bulk RNAseq dataset (n=2 samples) of actively translating transcripts in Stard5-expressing cells of the NAc generated using a Stard5-TRAP mouse line (BioProject PRJNA575143 (Heintz, 2019)). Paired-end FASTQ files were downloaded from the SRA using the `fastq-dump` function of the sratoolkit.

Read quality was inspected using FastQC (Andrews, 2024). Quality-based and length-based filtering and adapter removal were performed using fastp (Chen et al., 2018). Alignment was performed using the STAR aligner (Dobin et al., 2013) using the GENCODE (Frankish et al., 2021) mouse genome build GRCm39 (release M28). The output BAM files were filtered to the Stard5 region, and track plots generated in R using the package Gviz (Hahne and Ivanek, 2016). Sashimi plots were generated to visualize the total counts of transcripts that align to specific exons (histograms) and predicted splice junctions (curved lines). The sequencing library preparation was unstranded, preventing us from determining whether reads come from the sense or antisense strand. Hence, some of the Stard5 reads on the sense strand in the last exon of the Stard5-202 variant overlap with the IL16 gene on the antisense strand, making it impossible to deconvolute reads that map to Stard5 or IL16 in those overlapping regions, leading to artificial splice junctions across Stard5 and IL16. Still, despite these limitations, the results were unambiguous, showing a large proportion of the reads (total splice junction counts) mapping to the last exon of the Stard5-201 isoform (5742 reads mapped across both samples) rather than to the last two exons of the Stard5-202 isoform (246 reads) (**Supplementary Figure S4**). Hence the Stard5-201 transcript and its 3'UTR region are an adequate genomic region to be targeted. *Generation of the Stard5-2A-Flp0 transgenic mouse line.* The Stard5-2A-FlpO transgenic mouse line (official strain name: C57BL/6J-Stard5(2A-FLPo)Em1Ethz/Mlab) was created at the Transgenic Core of the ETH Phenomics Center. In this model, the FlpO gene, a mouse codon-optimized version of the FLP gene, was inserted at the C-terminus of the Stard5 gene. SV40 nuclear localization signal was included at its N-terminus. Gene expression was controlled via a 2A self-cleaving peptide (T2A) sequence, preceded by a Furin cleavage site (RA^KA), and terminated by the Stard5 polyA signal. To generate this transgenic line, gRNAs were designed using the CRISPOR algorithm (http://crispor.gi.ucsc.edu/) to target the region near the stop codon of the mouse Stard5 gene. The selected gRNA sequence was CAATAGGCGACTGTCAGTGA. A targeting template, 1962 bp in length, was used to facilitate homologous recombination (detailed sequence in Annex). This template was dialyzed against OmniPur® Water (Merck Millipore) and IDTE buffer (Integrated DNA Technologies) using a hydrophilic MCE filter membrane (0.22 µm pore size, Millipore Merck). The Stard5 sequence modification was achieved using CRISPR/Cas9 in 2-cell stage mouse embryos. Female C57BL/6J donors were primed for ovulation through intraperitoneal injections of 5 IU Pregnant Mare Serum Gonadotropin (PMSG, Novatein Bioscience), followed 48 hours later by 5 IU Human Chorionic Gonadotrophin (hCG) (Chorulon®, MSD Animal Health). Following hCG administration, females were mated with males of the same strain, and zygotes were collected from oviducts. Remaining cumulus cells were removed using a 5 min incubation in 0.3% Hyaluronidase (Sigma-Aldrich) in M2 medium (Sigma-Aldrich). Embryos were cultured overnight at 37°C and 5% CO2 in Embryomax KSOM medium (Sigma-Aldrich). Microinjections were performed on a microinjection system that included an inverted microscope with Nomarski optics (Leica), micromanipulators (Eppendorf), and a FemtoJet microinjection unit (Eppendorf). The injection mix contained IDTE buffer pH 7.5, annealed Alt-R™ CRISPR-Cas9 crRNA and tracrRNA (50 ng/µl), Alt-R S.p.Hifi-Cas9 Nuclease V3 (50 ng/µl), Alt-R™ HDR Enhancer V2 (1uM), and Alt-R™ HDR Donor Block double-stranded template (20 ng/µl) from IDT. Injection mix was filtered using Ultrafree®-MC column (Merck Millipore). After injection, surviving embryos were transferred into the oviducts of 8–20-week-old 0.5 days post coitus pseudopregnant CD-1 (RjOrl:SWISS) females mated with vasectomized males. Offspring genomic DNA was extracted from toe clip biopsies using the NucleoSpin Tissue kit (Macherey-Nagel) and analyzed for correct knock-in insertion via PCR using Phusion™ Plus DNA Polymerase (Thermo Fisher Scientific) and Sanger sequencing (Microsynth AG). The following primers were used for PCR: 5' GCACCTAGCTGTCCTACCAG 3' and 5' GATGTCGGTGATGTCGCTCT 3' (842 bp amplicon spanning the 5' homology arm) and 5' TCAGCAACAGCCTGAGCTTC 3' and 5' TACAGCAACCAGCACACAGG 3' (1403 bp amplicon spanning the 3' homology arm). Animals from the F2 generation onwards were used in experiments.

Metabolic cages and body composition of Stard5-Flp mice

Body composition was assessed using a quantitative nuclear magnetic resonance (NMR) scanner (Echo MRI-100H Body Composition Analyzer, Echo Medical Systems, Houston, USA) as previously described (Labouesse et al., 2018). Scans were performed by placing animals into a plastic cylinder, where they were kept immobile (no anesthesia) for the duration of the scan (20 s). Scans computed estimations of fat mass (all fat molecules in the body) and lean mass (all body parts containing water, excluding fat, bone minerals, free water and hair or cartilage). Indirect calorimetry measurements were performed with the Promethion metabolic cages (Sable Systems International) according to the manufacturer's guidelines and protocols. Energy expenditure analysis was performed by the Promethion software version using the Weir equation (Weir, 1949): EE = 3.9 x VO2 + 1.1 x VCO2 (kg/cal) where V02 and VC02 are the volume of oxygen and carbon dioxide (L) consumed and produced, respectively. The respiratory quotient was estimated by calculating the ratio of CO2 production to O2 consumption. Locomotor activity (infrared photobeam based monitoring), food and water intake were monitored throughout the whole measurement. Recordings were done at 22°C. Animals were single-caged. Data were collected and averaged from 3 consecutive days after an initial 1-3 days acclimatization period to the cages and the single-caging. Data was analyzed using the CalR application (Mina et al., 2018).

Surgical Procedures

Stereotaxic surgery was performed on a mouse stereotaxic apparatus (Stoelting) using glass pipettes pulled on a Universal Puller (DMZ Zeitz), a Nanoject II (Drummond) and a stereomicroscope (Kaps Optik SOM 82). Fibers were secured in place with miniscrews (FST), iBond (Demadent), dental cement (Charisma A2, Kulzer and Tetric EvoFlow, Ivoclar Vivadent; Demadent) cured with UV light (Woodpecker), and the skin closed with Vetbond (3M). Photometry fibers (2.5mm, 400 µm, 0.5 NA; R-FOC-BF400C-50NA) and optogenetic fibers (1.25mm, 200 µm, 0.22 NA; R-FOC-L200C-22NA) were purchased from RWD. Drd1-cre mice were injected unilaterally with 230 nL of AAV9-CAG-Flex-Synaptophysin-jGCaMP8s for tracing (self-production via ETH VVPP, order 037, titer 2.5 x10^12, originally generated in (Labouesse et al., 2023)) or AAV5-hSyn-Flex-jGCaMP8m for photometry (VVF Zurich v628-5, titer 8.1 x 10E12 vg/mL, diluted 2x in PBS), at AP +1.5, ML +0.5, DV -4.6, 4.4, 4.2 mm from bregma for the rostral medNAcSh and AP +1.0, ML +0.6, DV -4.8, -4.6, -4.5 for the caudal NAcSh. Photometry fibers were implanted at DV -4.3 (rostral medNAcSh) or DV -4.6 (caudal medNAcSh). For optogenetics, bilateral injections of 300 nL AAV5-hSyn-Flex-ChrimsonR (VVF Zurich v298-5, titer 5.2 x 10E12 vg/ml, undiluted) or AAV5-hSyn-Flex-mCherry (VVF v116-5, titer 7.5 x 10E12, undiluted) were done at AP +1.5, ML +0.5, DV -4.6, -4.4, -4.2 (rostral medNAcSh) or AP +1.0, ML +0.5, DV -4.6, -4.4, -4.2 (caudal medNAcSh) on both sides. Optogenetic fibers were implanted at the same AP, ML location at DV -4.2 [straight] and at AP +1.5, ML 0.5, DV-4.2 with an angle of 13.4° [angled] (rostral medNAcSh) and DV -4.2 [straight] and AP +1.0, ML 1.5, DV -4.2 with an angle of 13.4°[angled] (caudal medNAcSh). Stard5-Flp were injected with 300 nL of AAV2-CAG-dFRT-ratSynaptophysin-eGFP (VVF 780-2, titer 4.5 x 10E12 vg/mL, undiluted) and AAV1-hSyn-FRT-jGCaMP (VVF 740-1, titer 6.4 x 10E12 vg/ml, 2x diluted in PBS) for tracing the projections (**Supplementary Fig S6**) and for validation experiments/photometry, respectively, at the same coordinates as for the rostral medNAcSh above; or into the NAc core (AP 1.3, ML 1.35, DV -4.4) or dorsal striatum (AP +0.9, ML 1.5, DV -3.5). Behavioral experiments began 4-6 weeks after surgery. Animals for neuroanatomy were prepared >4 weeks after surgery. AAV and fiber locations were validated post-hoc.

Immunohistochemistry and neuroanatomical tracing

Mice were transcardially perfused with ice-cold 4% paraformaldehyde in PBS under deep anesthesia. For animals with fibers, skulls were immersed into PFA for 2-4 days. Brains were then extracted from PFA-fixed skulls and washed in PBS. Alternatively, brains were extracted after perfusion. Free-floating 50 µm coronal sections were immunostained using the following primary antibodies: chicken GFP (Abcam # ab13970, RRID AB_300798, used 1:1000), rabbit DsRed (Clontech, #632496, RRID AB_10013483, used 1:500-1:1000) and secondary antibodies from Thermofisher used 1:1000: 488 goat anti-chicken (A11039, RRID AB_2534096), 568 goat anti-rabbit (A-11036, RRID AB_10563566). Digital images were acquired using a Nikon Eclipse T2 epifluorescence microscope or an Olympus/Evident Slideview™ VS200 Slide Scanner, then processed with ImageJ.

Analysis of Allen Brain Atlas in-situ hybridization data

We used the open access resource Allen Brain Atlas (https://mouse.brain-map.org/) to identify molecular markers enriched in either the rostral or caudal medNAcSh. Available datasets were filtered for flagged expression in the NAc using the Fine Structure Search "nucleus accumbens". The markers included: 4932418E24Rik, Atp6v1c2, Calb1, Carhsp1, Cartpt, Ddit4l, Dlk1, Fxyd7, Gabrg3, Gpr12, Hpcal4, Hs6st2, Ids, Itgb1bp1, Kcng3, Kcnq5, Kctd4, Kctd8, Krt9, Lin7a, Lmo3, LOC381076, Lrrtm1, Lypd1, Man1a, MgII, Nrsn1, Pbx3, Peg10, Prkch, Prkg1, Rab27b, Rab3c, Rasal1, Rgs10, Sdc2, Sgsm1, Slc8a1, Smug1, Sorcs2, Stard5, Stra6, Sv2b, Tac2, Th, Zcchc12, Zdbf2, Zdhhc1. All 48 markers available were screened manually for a visibly strongly enriched expression in the rostral or caudal medNAcSh, also with good expression differences between the medNAcSh and neighboring regions (e.g. NAc core, NAc lateral shell and lateral septum). Quantification of marker expression in the medNAcSh was performed using optical density (OD) calculations in ImageJ. High-resolution coronal images (7-14 images spanning the rostral-caudal axis from AP +1.95 mm to +0.65 mm from bregma) from the Allen Brain Atlas (Allen Institute for Brain Science, 2004) for 1 dataset (1 animal) were downloaded and OD assessed within the regions of interest (ROI, medNAcSh, NAc core, lateral NAcSh, lateral septum) using 100 x 100 pixel squares on the raw unedited images. The data from both hemispheres (2 measures) were averaged for each ROI. OD values from the ROIs were subtracted from the average OD of the background (taken in the anterior commissure). For the purpose of the figure, images were edited in Microsoft PowerPoint, using contrast and brightness filters applied the same way to all images of the same staining, so as to improve staining visibility.

Analysis of scRNAseq data

To determine expression patterns of Stard5 and Peg10 in the NAc, we utilized a published scRNAseq dataset from the NAc (Chen et al., 2021). Gene expression matrix and metadata were downloaded from GEO (https://www.ncbi.nlm.nih.gov/geo/query/acc.cgi?acc=GSE118020) and imported into Seurat version 5.1.0 (Butler et al., 2018), using the 'min.cells' and 'min.features' parameters set to 3 and 1,250 respectively. Then the following functions were used: 'NormalizeData()' using the "LogNormalize" method with a scale factor of 1e6; 'ScaleData()' using 'nUMI', 'percent.mito', and 'Sample' as regression variables; 'FindVariableFeatures()' using the 'mean.var.plot' option, and mean and dispersion cutoffs from 1 to infinite. Then, PCA, UMAP, and tSNEs were computed, with UMAP and tSNE using the PCs 1:15. Separate objects for Drd1a+ (D1-SPN) and Drd2+ (D2-SPN) cells were generated, with the 'FindVariableFeatures()' and dimension reductions recomputed for each. Due to their relatively low expression in the dataset, cells were labelled in the Seurat metadata as either Stard5+, Drd1a+, Drd2+, or Peg10+, simply by the presence of a single copy of the respective gene in the main data assay. Feature plots of gene expression were generated using tSNE and the main data assay, with the 'FeaturePlot()' Seurat function. Proportions of the cells that were labelled as both Stard5 (or Peg10), and either Drd1a or Drd2 positive, were calculated by taking the number of cells that expressed both genes against the total number of cells. Proportions of the Stard5+ (or Peg10+) cells that are also either Drd1a+ or Drd2+ were

calculated by taking the number of Stard5+ (or Peg10+) cells divided by the number of those Stard5+ (or Peg10+) cells that were non-zero for the other gene. Data is pooled from 11 mice, 36670 cells.

Fluorescent in-situ hybridization assay

Stard5 and Peg10 expression patterns in NAc D1- and D2-SPNs was determined by fluorescent multiplex in-situ hybridization (RNAscope, Advanced Cell Diagnostics, CA, USA). Following rapid decapitation of wild-type mice, brains were rapidly frozen in powdered dry ice and stored at -80°C. Coronal sections of OCT-embedded brains were cut at 20 µm at -20°C and thaw-mounted onto Super Frost Plus slides (Fisher). Slides were stored at -80°C until further processing. Fluorescent in situ multiplex hybridization was performed according to the RNAscope Multiplex Fluorescent Reagent Kit v2 and the User Manual for fresh frozen tissue (Advanced Cell Diagnostics, Inc., CA, USA). Briefly, sections were fixed in 4% PFA, dehydrated with increasing percentage of EtOH, incubated with Hydrogen Peroxide and treated with protease III solution (Advanced Cell Diagnostics, Inc., CA, USA). Sections were then incubated with target probes for mouse Drd1 to label D1-SPNs (Drd1-C1, Cat No. 406491), mouse Drd2 to label D2-SPNs (Drd2-C2, Cat No. 406501-C2), mouse Stard5 to label Stard5+ cells (Stard5-C3, Cat No. 880931-C3) or Peg10 to label Peg10+ cells (Peg10-C3, Cat No. 512921-C3). Following probe hybridization, sections underwent a series of probe signal amplification steps followed by incubation of fluorescently labeled probes (TSA fluorophore detection kit, PerkinElmer, MA, USA) designed to target the specified channel associated with Stard5 or Peg10 (TSA Vivid Fluorophore 690), Drd1 (TSA Vivid Fluorophore 520) and Drd2 (TSA Vivid Fluorophore 570) as a triplex. Slides were counterstained with DAPI, and coverslipped with Fluoromount-G mounting medium (SouthernBiotech, Birmingham, AL, USA). High-resolution images (20X) were obtained on a fluorescent microscope (Olympus/Evident Slideview^{TM} VS200 Slide Scanner), exported and analyzed in Qupath-0.5.1 (Bankhead et al., 2017). Annotations were created for both hemispheres for the medNAcSh, lateral NAcSh and core. Cell detection was performed for each annotation using QuPath's built-in "Cell Detection" algorithm, with DAPI as the detection channel. The following nucleus parameters were used: background radius 8 µm, median filter radius 0 µm, sigma 1.2 µm, intensity threshold of 1000–3000, and cell expansion of 5 µm. Single measurement classifiers were created for all channels (FITC, Cy3, Cy5) to count the number of cells that were FITC+ (Drd1+ only), Cy3+ (Drd2+ only), Cy5+ (Stard5+ or Peg10+), or double/triple-positive. For each brain, 6-8 sections of the medNAcSh were included (covering rostral to caudal bregma levels +1.95 to +0.65 mm; on average 2-3 sections for most rostral and 2-3 sections for most caudal sections). Percent labeling was averaged for n=5 mice for Stard5 and n=5 for Peg10.

Fiber photometry

Fiber photometry was conducted using a RZ10X LUX-I/O Processor with integrated LEDs (Tucker-Davis Technologies) combined with a filter/mirror minicube set (FMC6_IE(400-410)_E1(467-497)_F1(507-554)_E2(566-586)_F2(600-680)_S) (Doric Lenses). The 405 nm LED was passed through a 400–410 nm bandpass filter, the 465 nm LED through a 467–497 nm GFP excitation filter, then both were coupled to a dichroic mirror to split excitation and emission lights. Low-autofluorescence patch cords (400 µm/0.57 NA, Doric) were attached to the optic fibers (400 µm/0.5 NA, RWD) on the mouse's head to collect fluorescence emissions. Signals were filtered through 507-554 nm GFP emission filters coupled to a photodetector on the RZ10X. Signals were sinusoidally modulated, using the TDT Synapse software at 210 and 330 Hz (405 and 465 nm, respectively) via a lock-in amplification detector, then demodulated and low-passed filtered at 6 Hz on-line. Data were sampled at 1017.3 Hz. 465 nm power at the patch cord was set to 30-35 µW.

Photometry recordings during reward consumption or unpredicted shock exposure

For behavioral experiments combined with medNAcSh photometry, an iCon behavior control interface (Tucker-Davis Technologies) was used to control an operant box (length 22 cm x width 20 cm x height 38 cm; ENV-307W-CT, Med Associates). The behavioral interface was directly connected to the RZ10X processor and controlled by custom-written codes written in Pynapse (version 96), a Python-based coding interface integrated into the TDT Synapse software. The iCon consisted of two modules – an iM10 multi-function interface and an iH16 28V control interface. The iM10 control interface contained the touch detector and received input from the lickometer. The iH16 controlled the retractable lickometer (ENV-352-2W Retractable Sipper Tube, Med Associates) and the aversive stimulator (ENV-414S, MedAssociates), house light and house fan. Mouse behavior was monitored using a camera (C270 HD webcam, Logitech) controlled by Synapse. The reward port access were custom-modified using a 3D printer to facilitate reward collection. For unpredicted reward delivery, mice were first trained across 7-10 days. On the first 2 days mice were given unrestricted access to the reward for 10 min followed by 10 min of restricted access with 10 s rewards being accessible at random intertrial intervals (ITIs) of 20-40 s. On days 3-5, mice were trained over 30 trials with the 10 s rewards accessible at random ITIs of 20-40 s. If the animal collected the reward within the specified reward windows, the trial was called a successful trial. If the mouse tried to collect the reward outside of the reward windows, a timeout period of 60 s was introduced during the training sessions. Once the mouse achieved a minimum of 10 successful trials, it was tethered for 2 days and trained similarly to days 3-5. After 10 successful trials, training was repeated for 3 days, with ITIs set at 30-50 s. Upon 12 successful trials, animals were tested in combination with in-vivo fiber photometry recordings under the same conditions. In case of >1 day break just before recordings (e.g. weekends), mice underwent an additional day of training before recording. For Drd1-cre mice, the experiment was repeated 3 times (all gave the same results; no learning effects), and the session on the last day was analyzed. For Stard5-Flp mice the experiment was conducted only once. For unpredicted shock, mice were exposed (without training) to 10 aversive shocks (0.4 mA, 1 s) with intertrial intervals of 40 to 80 s. Mice were placed inside a black-and-white striped cylinder in the operant box to create a context distinct from that of the reward experiment. A 3 min period at the beginning of all sessions with no stimuli were observed, and the data for these 3 min removed before analysis. MedNAcSh responses to reward consumption or to shock were quantified using custom in-house Matlab scripts as done previously (Labouesse et al., 2024, 2023). Data was 10x downsampled to 100 Hz and low-pass filtered (1 Hz). The first 3 min were trimmed to remove fast bleaching artefacts. Change in fluorescence, ΔF/F0 (%), was defined as (F-F0)/F0 x 100, where F represents the fluorescent signal (465 nm) at each time point. F0 was calculated by applying a least-squares linear fit (polyfit) to the 405 nm signal to align with the 465 nm signal, done on fluorescent data obtained in the -10 to +20 s around events. Event-related ΔF/F0 was baseline corrected against the ΔF/F0 average in the -10 to -1 s timewindow before event onset. Data was aligned to events of interest, namely the first lick during the 10 s window of reward availability or the shock onset. Average peri-stimulus time histogram (PSTH) curves generated by averaging the data from all mice within a session and heatmaps showing all trials in a session were computed showing the ΔF/F0 values (%) in windows of -5 to +20 s around events. Two epochs were used for analysis: the baseline epoch spanning -6 to -1 s before event start and event epoch spanning 0 to 5 s from event start. Area under the curve (AUC) was calculated for each epoch using the trapezoidal method. Peak maxima and minima ΔF/F0 were obtained by calculating the maxima or minima value for each epoch.

Optogenetic manipulations in a reward consumption task

Optogenetic stimulation was provided by a amber-light emitting laser (635 nm, Laserglow) and operant boxes and laser were driven using the iCon behavioral interface and custom-written Python code in Pynapse/Synapse software (TDT). Lasers were connected via optical patch cords (200 µm, 0.22 NA) and a rotary joint to the

animals' optic fibers. Rewards were available ad libitum via a lickometer (ENV-350CW, Med Associates). Initial training consisted of exposing mice to the lickometer during 3-5 sessions of 15-25 min. In the first two sessions mice were not tethered to the patch cord to facilitate training. Once the variability in lick counts across two consecutive sessions was less than 30 %, animals were moved to the test session. Two mice did not reach criterion and were excluded from the experiment. The proof-of-concept experiment consisted of three 8-min blocks, where laser stimulation occurred from minute 8 to minute 16. The stimulation was delivered continuously at 20 Hz (20 ms pulses, 10 mW power at fiber tip). The full optogenetic experiment consisted of five 5-min blocks, with laser stimulation during the first, third, and fifth blocks. Optogenetic stimulation was delivered continuously at 20 Hz (20 ms pulses, 300 µW power at fiber tip) throughout blocks 1, 3 and 5. All licks were detected with the Synapse software. Data was analyzed using custom-written Matlab codes to generate lick counts and lick counts/min.

Optogenetic manipulations in a real-time place preference and avoidance (RTPPA)

Optical stimulation was provided by a amber-light emitting laser (635 nm, Laserglow), which was activated using Anymaze version 7.37 (Stoelting). Lasers were connected via optical patch cords (200 µm, 0.22 NA) and a rotary joint to the animals' optic fibers. To activate ChrimsonR, we used 20 ms light pulses at 20 Hz with a power of 10 mW (or 300 µW, data not shown, results consistent) at the fiber tip. The RTPPA chamber consisted of 2 chambers of same dimension (30 x 30 x 30 cm, width, length, height) with different cues in each chamber. For the main experiment with 10 mW optogenetic laser power (shown in Figure 3), one chamber had thick vertical black stripes, while the other had horizontal ones. The experiment was repeated with lower laser power (300 µW) where we found the same results (data not shown): here, one chamber featured a black-and-white checkerboard pattern, and the other had diagonal black-and-white lines; experiment performed 5 months after the 10 mW one. Visual cues were also positioned outside the chamber. Testing consisted of 3 trials of 15 min each on 3 consecutive days. On day 1, animals were exposed to both sides of the chamber, and their preference was determined. Laser stimulation was assigned to the preferred chamber. On days 2 and 3, the laser was stimulated as soon as animals entered the laser-assigned chamber and for the entire duration of their visit. This was triggered in closed loop using a custom-written protocol in the Anymaze software. Time spent in each chamber was computed using Anymaze. Some animals were euthanized early to validate optic fiber surgery implantation; hence not all mice were used in both RTTPA and reward consumption tasks.

Statistics

Statistical analyses were performed using GraphPad Prism 9 or 10. Data are expressed as mean ± standard error of the mean (SEM). 2-group data were compared with paired or unpaired two-tailed Student's t-tests. Multiple comparisons were evaluated by ANOVA (no Greenhouse correction) and in the case of significant interactions, Sidak post-hoc tests were used. A p-value of <0.05 was considered statistically significant.

SUPPLEMENTARY INFORMATION

Supplementary Information includes 3 Datasets and 6 Figures, which can be found with this article online.

MATERIAL AVAILABILITY

The Stard5-Flp mouse is deposited at the ETH Phenomics Center (administration@epic.ethz.ch) in the form of cryopreserved straws (line 3072) under the group of Prof. Ferdinand von Meyenn (ETH). Its CRISPR sequence is available in **Supplementary Data S1**.

CODE AVAILABILITY

Original Python code to drive Pynapse is provided in **Supplementary Data S2**. Please cite this paper upon usage of the code. No new MATLAB code was developed but the original code can be found in (Labouesse et al., 2024, 2023).

DATA AVAILABILITY

Source data is provided as **Supplementary Data S3**.

ACKNOWLEDGEMENTS

This project was funded by the Swiss National Science Foundation (SNSF) (Ambizione Grant #PZ00P3_193430 to MAL) with additional support from the Brain and Behavior Research Foundation (Narsad Grant #30854) and the Novartis Foundation for Medical Biological Research (Grant #22B097). MAL received additional funding from the Vontobel Foundation (#1334/2021), the Olga Mayenfisch Foundation and an ETH Zurich Equipment Grant. AMM is funded by a PhD fellowship from the Zurich Neuroscience Center. CLF is funded by the SNSF (Grant #310030_207960). We thank Christian Wolfrum, Johannes Bohacek and Ferdinand von Meyenn for key infrastructural support; Johannes Bohacek, Theofannis Karayannis and Christopher Pryce for key scientific input; Ori Bar-Nur for access to fluorescent microscopy and Myrtha Arnold for support in the acquisition of key reagents. Some images were obtained from SciDraw under a CC-BY license (doi.org/10.5281/zenodo.3925917, doi.org/10.5281/zenodo.5496332 and doi.org/10.5281/zenodo.8319097).

AUTHOR CONTRIBUTIONS

AMM designed and conducted the experiments, performed the surgeries, wrote Python scripts for Pynapse, edited MATLAB scripts, analyzed data, supervised junior students and wrote the paper. EK wrote Python scripts for Pynapse and helped with in vivo photometry experiments, pilot anatomy experiments and data analysis. PL analyzed TRAPseq and scRNAseq data. KNB and CLF helped with proof-of-concept in vivo optogenetic experiments. MK helped with metabolic cage experiments and EchoMRI. NS designed and generated the Stard5-Flp mouse line. MAL acquired funding, established lab equipment, designed experiments, helped with pilot experiments, provided MATLAB scripts, analyzed data, wrote the paper and supervised the overall work. All authors contributed to the final version of the paper.

COMPETING INTERESTS

The authors have no competing interests to declare. With no relation to the present manuscript, MAL declares having been recently employed by Novartis.

MATERIALS AND CORRESPONDENCE

Further information and requests for resources and reagents should be directed to and will be fulfilled by the lead contact, Dr. Marie A. Labouesse (marie.labouesse@hest.ethz.ch).

REFERENCES

Adan, R.A.H., 2013. Mechanisms underlying current and future anti-obesity drugs. Trends Neurosci 36, 133–140. https://doi.org/10.1016/j.tins.2012.12.001

Al-Hasani, R., McCall, J.G., Shin, G., Gomez, A.M., Schmitz, G.P., Bernardi, J.M., Pyo, C.-O., Park, S.I., Marcinkiewcz, C.M., Crowley, N.A., Krashes, M.J., Lowell, B.B., Kash, T.L., Rogers, J.A., Bruchas, M.R., 2015. Distinct Subpopulations of Nucleus Accumbens Dynorphin Neurons Drive Aversion and Reward. Neuron 87, 1063–1077. https://doi.org/10.1016/j.neuron.2015.08.019

Andrews, S., 2024. FastQC: A Quality Control Tool for High Throughput Sequence Data.

Bankhead, P., Loughrey, M.B., Fernández, J.A., Dombrowski, Y., McArt, D.G., Dunne, P.D., McQuaid, S., Gray, R.T., Murray, L.J., Coleman, H.G., James, J.A., Salto-Tellez, M., Hamilton, P.W., 2017. QuPath: Open source software for digital pathology image analysis. Sci Rep 7, 16878. https://doi.org/10.1038/s41598-017-17204-5

Baumgartner, H.M., Cole, S.L., Olney, J.J., Berridge, K.C., 2020. Desire or Dread from Nucleus Accumbens Inhibitions: Reversed by Same-Site Optogenetic Excitations. J. Neurosci. 40, 2737–2752. https://doi.org/10.1523/JNEUROSCI.2902-19.2020

Bewernick, B.H., Hurlemann, R., Matusch, A., Kayser, S., Grubert, C., Hadrysiewicz, B., Axmacher, N., Lemke, M., Cooper-Mahkorn, D., Cohen, M.X., Brockmann, H., Lenartz, D., Sturm, V., Schlaepfer, T.E., 2010. Nucleus accumbens deep brain stimulation decreases ratings of depression and anxiety in treatment-resistant depression. Biol Psychiatry 67, 110–116. https://doi.org/10.1016/j.biopsych.2009.09.013

Bond, C.W., Trinko, R., Foscue, E., Furman, K., Groman, S.M., Taylor, J.R., DiLeone, R.J., 2020. Medial Nucleus Accumbens Projections to the Ventral Tegmental Area Control Food Consumption. J. Neurosci. 40, 4727–4738. https://doi.org/10.1523/JNEUROSCI.3054-18.2020

Butler, A., Hoffman, P., Smibert, P., Papalexi, E., Satija, R., 2018. Integrating single-cell transcriptomic data across different conditions, technologies, and species. Nat Biotechnol 36, 411–420. https://doi.org/10.1038/nbt.4096

Castro, Daniel C., Berridge, K.C., 2014. Opioid Hedonic Hotspot in Nucleus Accumbens Shell: Mu, Delta, and Kappa Maps for Enhancement of Sweetness “Liking” and “Wanting.” J. Neurosci. 34, 4239–4250. https://doi.org/10.1523/JNEUROSCI.4458-13.2014

Castro, D.C., Berridge, K.C., 2014. Advances in the neurobiological bases for food ‘liking’ versus ‘wanting.’ Physiol Behav 0, 22–30. https://doi.org/10.1016/j.physbeh.2014.05.022

Castro, D.C., Terry, R.A., Berridge, K.C., 2016. Orexin in Rostral Hotspot of Nucleus Accumbens Enhances Sucrose ‘Liking’ and Intake but Scopolamine in Caudal Shell Shifts ‘Liking’ Toward ‘Disgust’ and ‘Fear.’ Neuropsychopharmacol 41, 2101–2111. https://doi.org/10.1038/npp.2016.10

Chen, G., Lai, S., Bao, G., Ke, J., Meng, X., Lu, S., Wu, X., Xu, H., Wu, F., Xu, Y., Xu, F., Bi, G.-Q., Peng, G., Zhou, K., Zhu, Y., 2023. Distinct reward processing by subregions of the nucleus accumbens. Cell Reports 42, 112069. https://doi.org/10.1016/j.celrep.2023.112069

Chen, R., Blosser, T.R., Djekidel, M.N., Hao, J., Bhattacherjee, A., Chen, W., Tuesta, L.M., Zhuang, X., Zhang, Y., 2021. Decoding molecular and cellular heterogeneity of mouse nucleus accumbens. Nat Neurosci 1–15. https://doi.org/10.1038/s41593-021-00938-x

Chen, S., Zhou, Y., Chen, Y., Gu, J., 2018. fastp: an ultra-fast all-in-one FASTQ preprocessor. Bioinformatics 34, i884–i890. https://doi.org/10.1093/bioinformatics/bty560

Corre, J., van Zessen, R., Loureiro, M., Patriarchi, T., Tian, L., Pascoli, V., Lüscher, C., 2018. Dopamine neurons projecting to medial shell of the nucleus accumbens drive heroin reinforcement. Elife 7, e39945. https://doi.org/10.7554/eLife.39945

Creed, M., Pascoli, V.J., Lüscher, C., 2015. Refining deep brain stimulation to emulate optogenetic treatment of synaptic pathology. Science 347, 659–664. https://doi.org/10.1126/science.1260776

de Jong, J.W., Afjei, S.A., Pollak Dorocic, I., Peck, J.R., Liu, C., Kim, C.K., Tian, L., Deisseroth, K., Lammel, S., 2019. A Neural Circuit Mechanism for Encoding Aversive Stimuli in the Mesolimbic Dopamine System. Neuron 101, 133-151.e7. https://doi.org/10.1016/j.neuron.2018.11.005

Domingues, A.V., Carvalho, T.T.A., Martins, G.J., Correia, R., Coimbra, B., Bastos-Gonçalves, R., Wezik, M., Gaspar, R., Pinto, L., Sousa, N., Costa, R.M., Soares-Cunha, C., Rodrigues, A.J., 2025. Dynamic representation of appetitive and aversive stimuli in nucleus accumbens shell D1- and D2-medium spiny neurons. Nat Commun 16, 59. https://doi.org/10.1038/s41467-024-55269-9

Faure, A., Richard, J.M., Berridge, K.C., 2010. Desire and Dread from the Nucleus Accumbens: Cortical Glutamate and Subcortical GABA Differentially Generate Motivation and Hedonic Impact in the Rat. PLOS ONE 5, e11223. https://doi.org/10.1371/journal.pone.0011223

Fischer, K.B., Collins, H.K., Callaway, E.M., 2019. Sources of off-target expression from recombinase-dependent AAV vectors and mitigation with cross-over insensitive ATG-out vectors. Proc Natl Acad Sci U S A 116, 27001–27010. https://doi.org/10.1073/pnas.1915974116

Frankish, A., Diekhans, M., Jungreis, I., Lagarde, J., Loveland, J.E., Mudge, J.M., Sisu, C., Wright, J.C., Armstrong, J., Barnes, I., Berry, A., Bignell, A., Boix, C., Carbonell Sala, S., Cunningham, F., Di Domenico, T., Donaldson, S., Fiddes, I.T., García Girón, C., Gonzalez, J.M., Grego, T., Hardy, M., Hourlier, T., Howe, K.L., Hunt, T., Izuogu, O.G., Johnson, R., Martin, F.J., Martínez, L., Mohanan, S., Muir, P., Navarro, F.C.P., Parker, A., Pei, B., Pozo, F., Riera, F.C., Ruffier, M., Schmitt, B.M., Stapleton, E., Suner, M.-M., Sycheva, I., Uszczynska-Ratajczak, B., Wolf, M.Y., Xu, J., Yang, Y.T., Yates, A., Zerbino, D., Zhang, Y., Choudhary, J.S., Gerstein, M., Guigó, R., Hubbard, T.J.P., Kellis, M., Paten, B., Tress, M.L., Flicek, P., 2021. GENCODE 2021. Nucleic Acids Res 49, D916–D923. https://doi.org/10.1093/nar/gkaa1087

Gibson, G.D., Prasad, A.A., Jean-Richard-dit-Bressel, P., Yau, J.O.Y., Millan, E.Z., Liu, Y., Campbell, E.J., Lim, J., Marchant, N.J., Power, J.M., Killcross, S., Lawrence, A.J., McNally, G.P., 2018. Distinct Accumbens Shell Output Pathways Promote versus Prevent Relapse to Alcohol Seeking. Neuron 98, 512-520.e6. https://doi.org/10.1016/j.neuron.2018.03.033

Hahne, F., Ivanek, R., 2016. Visualizing Genomic Data Using Gviz and Bioconductor. Methods Mol Biol 1418, 335–351. https://doi.org/10.1007/978-1-4939-3578-9_16

Heintz, N., 2019. Transcriptional profiling of neurons in the ventra... (ID 575143) - BioProject - NCBI.

Hintiryan, H., Foster, N.N., Bowman, I., Bay, M., Song, M.Y., Gou, L., Yamashita, S., Bienkowski, M.S., Zingg, B., Zhu, M., Yang, X.W., Shih, J.C., Toga, A.W., Dong, H.-W., 2016. The mouse cortico-striatal projectome. Nat Neurosci 19, 1100–1114. https://doi.org/10.1038/nn.4332

Hounchonou, H.F., Tang, H., Paulat, R., Kühn, A., Spranger, J., van Riesen, C., Maurer, L., 2023. Continuous deep brain stimulation of the nucleus accumbens reduces food intake but does not affect body weight in mice fed a high-fat diet. Sci Rep 13, 18952. https://doi.org/10.1038/s41598-023-45511-7

Kelley, A.E., Baldo, B.A., Pratt, W.E., 2005. A proposed hypothalamic-thalamic-striatal axis for the integration of energy balance, arousal, and food reward. J Comp Neurol 493, 72–85. https://doi.org/10.1002/cne.20769

Krause, M., German, P.W., Taha, S.A., Fields, H.L., 2010. A Pause in Nucleus Accumbens Neuron Firing Is Required to Initiate and Maintain Feeding. J. Neurosci. 30, 4746–4756. https://doi.org/10.1523/JNEUROSCI.0197-10.2010

Labouesse, M.A., Sartori, A.M., Weinmann, O., Simpson, E.H., Kellendonk, C., Weber-Stadlbauer, U., 2018. Striatal dopamine 2 receptor upregulation during development predisposes to diet-induced obesity by reducing energy output in mice. Proc. Natl. Acad. Sci. U.S.A. 115, 10493–10498. https://doi.org/10.1073/pnas.1800171115

Labouesse, M.A., Stadlbauer, U., Weber, E., Arnold, M., Langhans, W., Pacheco-López, G., 2012. Vagal afferents mediate early satiation and prevent flavour avoidance learning in response to intraperitoneally infused exendin-4. J Neuroendocrinol 24, 1505–1516. https://doi.org/10.1111/j.1365-2826.2012.02364.x

Labouesse, M.A., Torres-Herraez, A., Chohan, M.O., Villarin, J.M., Greenwald, J., Sun, X., Zahran, M., Tang, A., Lam, S., Veenstra-VanderWeele, J., Lacefield, C.O., Bonaventura, J., Michaelides, M., Chan, C.S., Yizhar, O., Kellendonk, C., 2023. A non-canonical striatopallidal Go pathway that supports motor control. Nat Commun 14, 6712. https://doi.org/10.1038/s41467-023-42288-1

Labouesse, M.A., Wilhelm, M., Kagiampaki, Z., Yee, A.G., Denis, R., Harada, M., Gresch, A., Marinescu, A.-M., Otomo, K., Curreli, S., Serratosa Capdevila, L., Zhou, Xuehan, Cola, R.B., Ravotto, L., Glück, C., Cherepanov, S., Weber, B., Zhou, Xin, Katner, J., Svensson, K.A., Fellin, T., Trudeau, L.-E., Ford, C.P., Sych, Y., Patriarchi, T., 2024. A chemogenetic approach for dopamine imaging with tunable sensitivity. Nat Commun 15, 5551. https://doi.org/10.1038/s41467-024-49442-3

Liu, Y., Wang, Y., Zhao, Z., Xie, G., Zhang, C., Chen, R., Zhang, Y., 2024. A subset of dopamine receptor-expressing neurons in the nucleus accumbens controls feeding and energy homeostasis. Nat Metab 6, 1616–1631. https://doi.org/10.1038/s42255-024-01100-0

Liu, Z., Le, Q., Lv, Y., Chen, X., Cui, J., Zhou, Y., Cheng, D., Ma, C., Su, X., Xiao, L., Yang, R., Zhang, J., Ma, L., Liu, X., 2022. A distinct D1-MSN subpopulation down-regulates dopamine to promote negative emotional state. Cell Res 32, 139–156. https://doi.org/10.1038/s41422-021-00588-5

Lüscher, C., Janak, P.H., 2021. Consolidating the Circuit Model for Addiction. Annu Rev Neurosci 44, 173–195. https://doi.org/10.1146/annurev-neuro-092920-123905

Maldonado-Irizarry, C., Swanson, C., Kelley, A., 1995. Glutamate receptors in the nucleus accumbens shell control feeding behavior via the lateral hypothalamus. J. Neurosci. 15, 6779–6788. https://doi.org/10.1523/JNEUROSCI.15-10-06779.1995

Marinescu, A.-M., Labouesse, M.A., 2024. The nucleus accumbens shell: a neural hub at the interface of homeostatic and hedonic feeding. Front. Neurosci. 18. https://doi.org/10.3389/fnins.2024.1437210

Matikainen-Ankney, B.A., Legaria, A.A., Pan, Y., Vachez, Y.M., Murphy, C.A., Schaefer, R.F., McGrath, Q.J., Wang, J.G., Bluitt, M.N., Ankney, K.C., Norris, A.J., Creed, M.C., Kravitz, A.V., 2023. Nucleus Accumbens D1 Receptor-Expressing Spiny Projection Neurons Control Food Motivation and Obesity. Biol Psychiatry 93, 512–523. https://doi.org/10.1016/j.biopsych.2022.10.003

Mina, A.I., LeClair, R.A., LeClair, K.B., Cohen, D.E., Lantier, L., Banks, A.S., 2018. *CalR*: A Web-Based Analysis Tool for Indirect Calorimetry Experiments. Cell Metabolism 28, 656-666.e1. https://doi.org/10.1016/j.cmet.2018.06.019

Müller, T.D., Blüher, M., Tschöp, M.H., DiMarchi, R.D., 2022. Anti-obesity drug discovery: advances and challenges. Nat Rev Drug Discov 21, 201–223. https://doi.org/10.1038/s41573-021-00337-8

Nho, Y.-H., Rolle, C.E., Topalovic, U., Shivacharan, R.S., Cunningham, T.N., Hiller, S., Batista, D., Feng, A., Espil, F.M., Kratter, I.H., Bhati, M.T., Kellogg, M., Raslan, A.M., Williams, N.R., Garnett, J., Pesaran, B., Oathes, D.J., Suthana, N., Barbosa, D.A.N., Halpern, C.H., 2024. Responsive deep brain stimulation guided by ventral striatal electrophysiology of obsession durably ameliorates compulsion. Neuron 112, 73-83.e4. https://doi.org/10.1016/j.neuron.2023.09.034

O'Connor, E.C., Kremer, Y., Lefort, S., Harada, M., Pascoli, V., Rohner, C., Lüscher, C., 2015. Accumbal D1R Neurons Projecting to Lateral Hypothalamus Authorize Feeding. Neuron 88, 553–564. https://doi.org/10.1016/j.neuron.2015.09.038

Pedersen, C.E., Castro, D.C., Gray, M.M., Zhou, Z.C., Piantadosi, S.C., Gowrishankar, R., Kan, S.A., Murphy, P.J., O'Neill, P.R., Bruchas, M.R., 2022. Medial accumbens shell spiny projection neurons encode relative reward preference. https://doi.org/10.1101/2022.09.18.508426

Pisanello, F., Mandelbaum, G., Pisanello, M., Oldenburg, I.A., Sileo, L., Markowitz, J.E., Peterson, R.E., Della Patria, A., Haynes, T.M., Emara, M.S., Spagnolo, B., Datta, S.R., De Vittorio, M., Sabatini, B.L., 2017. Dynamic illumination of spatially restricted or large brain volumes via a single tapered optical fiber. Nat Neurosci 20, 1180–1188. https://doi.org/10.1038/nn.4591

Piwecka, M., Rajewsky, N., Rybak-Wolf, A., 2023. Single-cell and spatial transcriptomics: deciphering brain complexity in health and disease. Nat Rev Neurol 19, 346–362. https://doi.org/10.1038/s41582-023-00809-y

Reed, S.J., Lafferty, C.K., Mendoza, J.A., Yang, A.K., Davidson, T.J., Grosenick, L., Deisseroth, K., Britt, J.P., 2018. Coordinated Reductions in Excitatory Input to the Nucleus Accumbens Underlie Food Consumption. Neuron 99, 1260-1273.e4. https://doi.org/10.1016/j.neuron.2018.07.051

Reynolds, S.M., Berridge, K.C., 2008. Emotional environments retune the valence of appetitive versus fearful functions in nucleus accumbens. Nat Neurosci 11, 423–425. https://doi.org/10.1038/nn2061

Reynolds, S.M., Berridge, K.C., 2002. Positive and Negative Motivation in Nucleus Accumbens Shell: Bivalent Rostrocaudal Gradients for GABA-Elicited Eating, Taste "Liking"/"Disliking" Reactions, Place Preference/Avoidance, and Fear. J. Neurosci. 22, 7308–7320. https://doi.org/10.1523/JNEUROSCI.22-16-07308.2002

Reynolds, S.M., Berridge, K.C., 2001. Fear and Feeding in the Nucleus Accumbens Shell: Rostrocaudal Segregation of GABA-Elicited Defensive Behavior Versus Eating Behavior. J. Neurosci. 21, 3261–3270. https://doi.org/10.1523/JNEUROSCI.21-09-03261.2001

Richard, J.M., Berridge, K.C., 2011. Nucleus Accumbens Dopamine/Glutamate Interaction Switches Modes to Generate Desire versus Dread: D1 Alone for Appetitive Eating But D1 and D2 Together for Fear. J. Neurosci. 31, 12866–12879. https://doi.org/10.1523/JNEUROSCI.1339-11.2011

Richard, J.M., Plawecki, A.M., Berridge, K.C., 2013. Nucleus accumbens GABAergic inhibition generates intense eating and fear that resists environmental retuning and needs no local dopamine. European Journal of Neuroscience 37, 1789–1802. https://doi.org/10.1111/ejn.12194

Roitman, M.F., Wheeler, R.A., Carelli, R.M., 2005. Nucleus Accumbens Neurons Are Innately Tuned for Rewarding and Aversive Taste Stimuli, Encode Their Predictors, and Are Linked to Motor Output. Neuron 45, 587–597. https://doi.org/10.1016/j.neuron.2004.12.055

Rossi, M.A., 2023. Control of energy homeostasis by the lateral hypothalamic area. Trends Neurosci 46, 738–749. https://doi.org/10.1016/j.tins.2023.05.010

Shivacharan, R.S., Rolle, C.E., Barbosa, D.A.N., Cunningham, T.N., Feng, A., Johnson, N.D., Safer, D.L., Bohon, C., Keller, C., Buch, V.P., Parker, J.J., Azagury, D.E., Tass, P.A., Bhati, M.T., Malenka, R.C., Lock, J.D., Halpern, C.H., 2022. Pilot study of responsive nucleus accumbens deep brain stimulation for loss-of-control eating. Nat Med 28, 1791–1796. https://doi.org/10.1038/s41591-022-01941-w

Stanley, G., Gokce, O., Malenka, R.C., Südhof, T.C., Quake, S.R., 2020. Continuous and Discrete Neuron Types of the Adult Murine Striatum. Neuron 105, 688-699.e8. https://doi.org/10.1016/j.neuron.2019.11.004

Stratford, T.R., Kelley, A.E., 1999. Evidence of a Functional Relationship between the Nucleus Accumbens Shell and Lateral Hypothalamus Subserving the Control of Feeding Behavior. J. Neurosci. 19, 11040–11048. https://doi.org/10.1523/JNEUROSCI.19-24-11040.1999

Stratford, T.R., Kelley, A.E., 1997. GABA in the Nucleus Accumbens Shell Participates in the Central Regulation of Feeding Behavior. J. Neurosci. 17, 4434–4440. https://doi.org/10.1523/JNEUROSCI.17-11-04434.1997

Stuber, G.D., Schwitzgebel, V.M., Lüscher, C., 2025. The neurobiology of overeating. Neuron. https://doi.org/10.1016/j.neuron.2025.03.010

Taha, S.A., Fields, H.L., 2006. Inhibitions of nucleus accumbens neurons encode a gating signal for reward-directed behavior. J Neurosci 26, 217–222. https://doi.org/10.1523/JNEUROSCI.3227-05.2006

Taha, S.A., Fields, H.L., 2005. Encoding of Palatability and Appetitive Behaviors by Distinct Neuronal Populations in the Nucleus Accumbens. J. Neurosci. 25, 1193–1202. https://doi.org/10.1523/JNEUROSCI.3975-04.2005

Thoeni, S., Loureiro, M., O'Connor, E.C., Lüscher, C., 2020. Depression of Accumbal to Lateral Hypothalamic Synapses Gates Overeating. Neuron 107, 158-172.e4. https://doi.org/10.1016/j.neuron.2020.03.029

Trouche, S., Koren, V., Doig, N.M., Ellender, T.J., El-Gaby, M., Lopes-dos-Santos, V., Reeve, H.M., Perestenko, P.V., Garas, F.N., Magill, P.J., Sharott, A., Dupret, D., 2019. A Hippocampus-Accumbens Tripartite Neuronal Motif Guides Appetitive Memory in Space. Cell 176, 1393-1406.e16. https://doi.org/10.1016/j.cell.2018.12.037

Vachez, Y.M., Tooley, J.R., Abiraman, K., Matikainen-Ankney, B., Casey, E., Earnest, T., Ramos, L.M., Silberberg, H., Godynyuk, E., Uddin, O., Marconi, L., Le Pichon, C.E., Creed, M.C., 2021. Ventral arkypallidal neurons inhibit accumbal firing to promote reward consumption. Nature Neuroscience 24, 379–390. https://doi.org/10.1038/s41593-020-00772-7

Valjent, E., Gangarossa, G., 2021. The Tail of the Striatum: From Anatomy to Connectivity and Function. Trends in Neurosciences 44, 203–214. https://doi.org/10.1016/j.tins.2020.10.016

Walle, R., Petitbon, A., Fois, G.R., Varin, C., Montalban, E., Hardt, L., Contini, A., Angelo, M.F., Potier, M., Ortole, R., Oummadi, A., De Smedt-Peyrusse, V., Adan, R.A., Giros, B., Chaouloff, F., Ferreira, G., de Kerchove d'Exaerde, A., Ducrocq, F., Georges, F., Trifilieff, P., 2024. Nucleus accumbens D1- and D2-expressing neurons control the balance between feeding and activity-mediated energy expenditure. Nat Commun 15, 2543. https://doi.org/10.1038/s41467-024-46874-9

Weir, J.B. de V., 1949. New methods for calculating metabolic rate with special reference to protein metabolism. The Journal of Physiology 109, 1–9. https://doi.org/10.1113/jphysiol.1949.sp004363

Xu, L., Nan, J., Lan, Y., 2020. The Nucleus Accumbens: A Common Target in the Comorbidity of Depression and Addiction. Front. Neural Circuits 14. https://doi.org/10.3389/fncir.2020.00037

Yang, H., de Jong, J.W., Tak, Y., Peck, J., Bateup, H.S., Lammel, S., 2018. Nucleus Accumbens Subnuclei Regulate Motivated Behavior via Direct Inhibition and Disinhibition of VTA Dopamine Subpopulations. Neuron 97, 434-449.e4. https://doi.org/10.1016/j.neuron.2017.12.022

Zhang, C., Wei, N.-L., Wang, Y., Wang, X., Zhang, J.-G., Zhang, K., 2015. Deep brain stimulation of the nucleus accumbens shell induces anti-obesity effects in obese rats with alteration of dopamine neurotransmission. Neuroscience Letters 589, 1–6. https://doi.org/10.1016/j.neulet.2015.01.019

Zhang, M., Pan, X., Jung, W., Halpern, A.R., Eichhorn, S.W., Lei, Z., Cohen, L., Smith, K.A., Tasic, B., Yao, Z., Zeng, H., Zhuang, X., 2023. Molecularly defined and spatially resolved cell atlas of the whole mouse brain. Nature 624, 343–354. https://doi.org/10.1038/s41586-023-06808-9

Zhang, Y., Rózsa, M., Liang, Y., Bushey, D., Wei, Z., Zheng, J., Reep, D., Broussard, G.J., Tsang, A., Tsegaye, G., Narayan, S., Obara, C.J., Lim, J.-X., Patel, R., Zhang, R., Ahrens, M.B., Turner, G.C., Wang, S.S.-H., Korff, W.L., Schreiter, E.R., Svoboda, K., Hasseman, J.P., Kolb, I., Looger, L.L., 2023. Fast and sensitive GCaMP calcium indicators for imaging neural populations. Nature 615, 884–891. https://doi.org/10.1038/s41586-023-05828-9

Zhao, Z., Han, X., Chen, R., Liu, Y., Bhattacherjee, A., Chen, W., Zhang, Y., 2022. A molecularly defined D1 medium spiny neuron subtype negatively regulates cocaine addiction. Science Advances 8, eabn3552. https://doi.org/10.1126/sciadv.abn3552

Zhou, K., Xu, H., Lu, S., Jiang, S., Hou, G., Deng, X., He, M., Zhu, Y., 2022. Reward and aversion processing by input-defined parallel nucleus accumbens circuits in mice. Nat Commun 13, 6244. https://doi.org/10.1038/s41467-022-33843-3

Zhu, Z., Gong, R., Rodriguez, V., Quach, K.T., Chen, X., Sternson, S.M., 2025. Hedonic eating is controlled by dopamine neurons that oppose GLP-1R satiety. Science 387, eadt0773. https://doi.org/10.1126/science.adt0773

SUPPLEMENTARY FIGURES

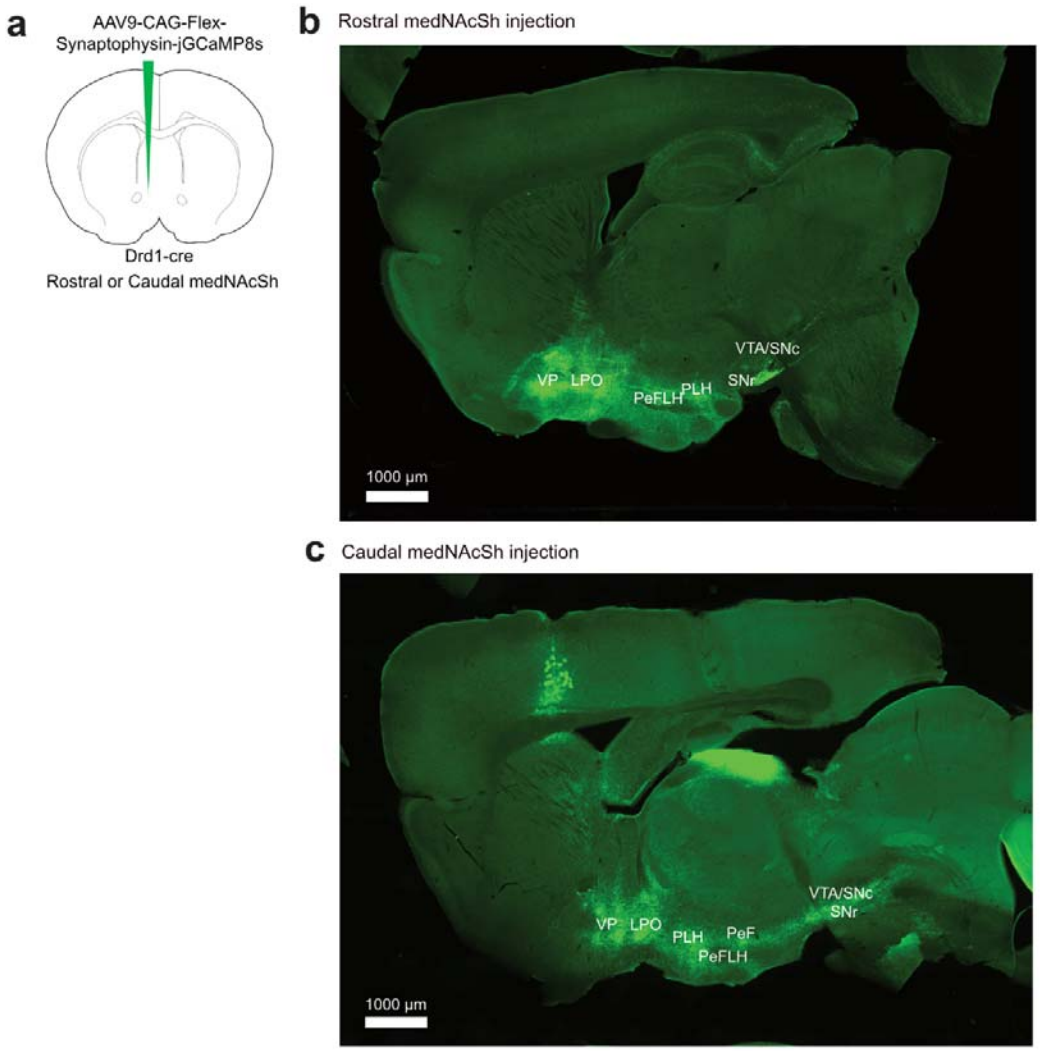

Supplementary Figure S1. Projections sites of D1-SPNs from the rostral and caudal medNAcSh. a. Surgery schematics of Drd1-cre mice injected with a cre-dependent green anterograde tracer (Synaptophysin-jGCaMP8s) in the rostral or caudal medNAcSh to trace projections **b.** Representative sagittal images of rostral (upper panel) vs. caudal (lower) medNAcSh mice injected with the tracer. Axons arising from rostral vs. caudal medNAcSh D1-SPNs both similarly reach the canonical target regions of D1-SPNs, namely the ventral pallidum (VP), lateral hypothalamus (LH) region (includes the perifornical nucleus: PeF, PLH: peduncular part of lateral hypothalamus), the lateral preoptic area (LPO), which is closely connected with the LH and the midbrain (includes VTA: ventral tegmental area /SNc: substantia nigra compacta, and SNr: substantia nigra compacta). Related to **Figures 1, 2, 3**. See also **Supplementary Figure S6**.

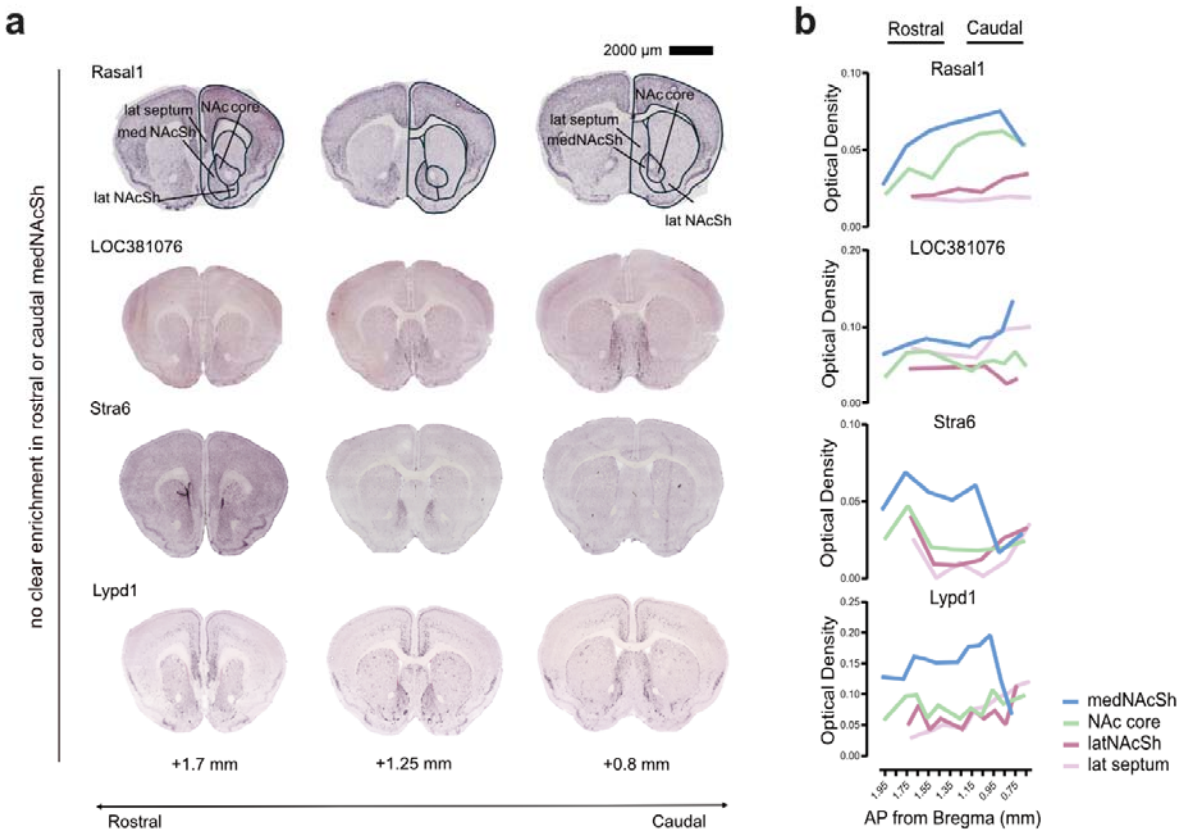

Supplementary Figure S2. Molecular markers for the medNAcSh. a. Representative in-situ hybridization images obtained from the Allen Brain Atlas (https://mouse.brain-map.org/) for markers showing no clear enriched expression in the rostral vs. caudal medNAcSh. All 48 markers available in the Allen Brain Atlas labeling the nucleus accumbens were screened, and most showed no clear enrichment pattern for the medNAcSh. Representative markers (Rasal1, LOC381076, Stra6, Lypd1) are shown here. Images on the left are more rostral (bregma +1.65 mm); images on the right are more caudal (bregma +0.85 mm). **b.** Quantification of expression levels of relevant markers in the medNAcSh along the rostral-caudal axis (bregma +1.95 mm to +0.75 mm) using optical density measurements (n = 1 mouse, 7-14 sections total, data shown is the mean from 2 measures/section) showing no clear enrichment in the rostral or caudal medNAcSh for the 4 markers. Data for the NAc core, lateral NAcSh (lat NAcSh) and lateral septum (lat septum) are also shown. Related to **Figure 4**.

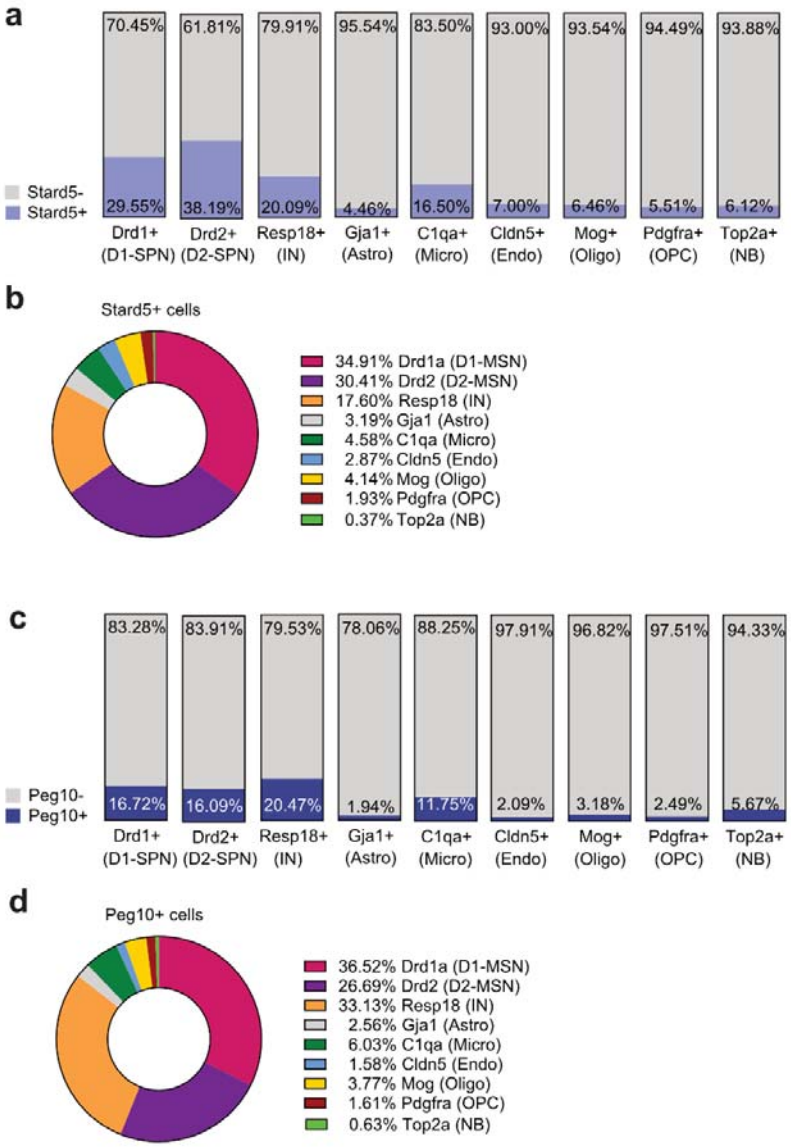

Supplementary Figure S3. Stard5 and Peg10 expression patterns in the NAc. a. Percent expression of cells positive (+) or negative (-) for Stard5 in various cell types in the entire nucleus accumbens (NAc) (i.e. not only the medNAcSh like in our RNAscope analysis in **Fig 5d-g**), based on re-analysis of a published scRNAseq dataset: GSE118020 (Chen et al., 2021) (same dataset as in **Fig 5a-b**). This shows that ~30-40% of D1-SPNs and D2-SPNs express Stard5; ~20% of interneurons express Stard5. **b.** Expression of cell type canonical markers within all nucleus accumbens Stard5+ cells. Some cells express >1 marker; hence total % can be >100%. This shows that D1-SPNs and D2-SPNs represent the majority of Stard5+ cells (~30-35% each), while interneurons represent 17%. Cell types are identified by canonical markers, the same used in (Chen et al., 2021). **c.** Percent expression of cells positive (+) or negative (-) for Peg10 in various cell types in the entire nucleus accumbens based on re-analysis of a published scRNAseq dataset: GSE118020 (Chen et al., 2021). This shows that ~20% of interneurons express Peg10; around 16% of D1-SPNs and of D2-SPNs express Peg10. **d.** Expression of cell type canonical markers within all nucleus accumbens Peg10+ cells. Some cells express >1 marker; hence total % can be >100%. This shows that D1-SPNs, D2-SPNs and interneurons represent the majority of Peg10+ cells (about 1/3 each). Cell types are identified by canonical markers, the same used in (Chen et al., 2021). Drd1 labels dopamine 1 receptor+ SPNs, Drd2 labels dopamine 2 receptor+ SPNs, Resp18 labels interneurons, Gja1 labels astrocytes, C1qa labels microglia, Cldn5 labels endothelial cells, Mog labels oligodendrocytes, Pdgfra labels oligodendrocyte progenitor cells, Top2a labels neural stem cells and neuroblasts. Related to **Figure 5**.

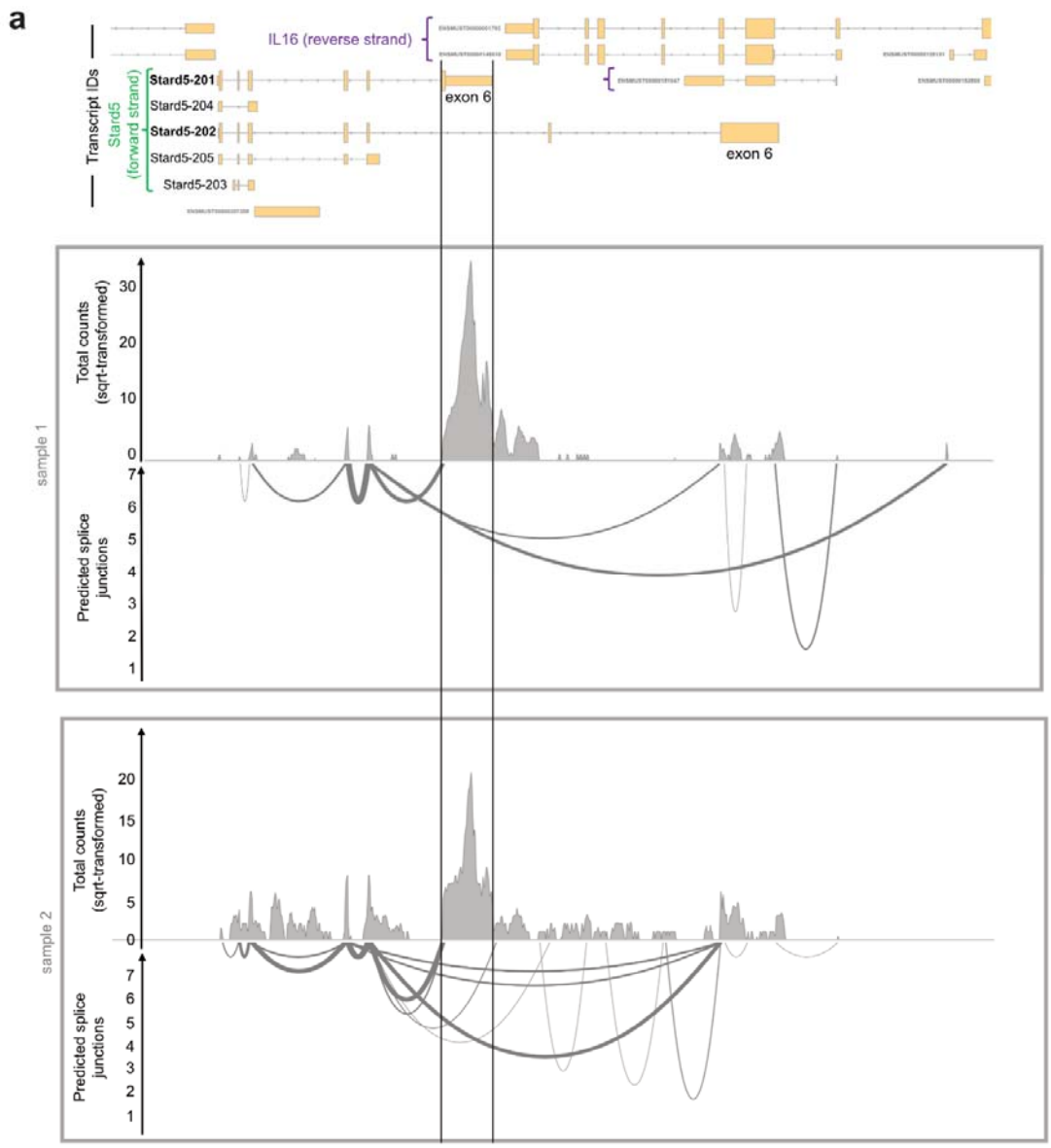

Supplementary Figure S4. Stard5-201 is the dominant splice variant expressed in the NAc, making it an adequate genomic region for 2A-Flp0 vector targeting (Stard5-Flp mouse line generation). StAR-related lipid transfer (START) domain containing 5 (Stard5) is a gene located on mouse chromosome 7, distributed over 6 exons, coding for a protein of 213 amino acid residues (transcript Stard5-201; ID: ENSMUST00000075418.15). In addition, there are 4 more registered transcripts out of which only one more has an open reading frame (transcript Stard5-202; ID: ENSMUST00000117410.2, encoding for a 206aa protein). **a.** Data is obtained from TRAP-seq data from actively transcribing transcripts in Stard5+ cells in the NAc, using a Stard5-TRAP mouse line. Sashimi plot showing the isoform model of the GENCODE GRCm39 reference genome and transcript IDs [top], the read mapping abundance (square-root transformed) [middle], and the splice junction abundance (square-root transformed) [bottom] for samples 1 and 2. A large proportion of the reads (total splice junction counts) mapped to the last exon of the Stard5-201 isoform (5742 reads mapped across both samples) rather than to the last two exons of the Stard5-202 isoform (246 reads), indicating Stard5-201 is the dominant splice variant expressed in Stard5+ cells in the NAc. Related to **Figure 6**.

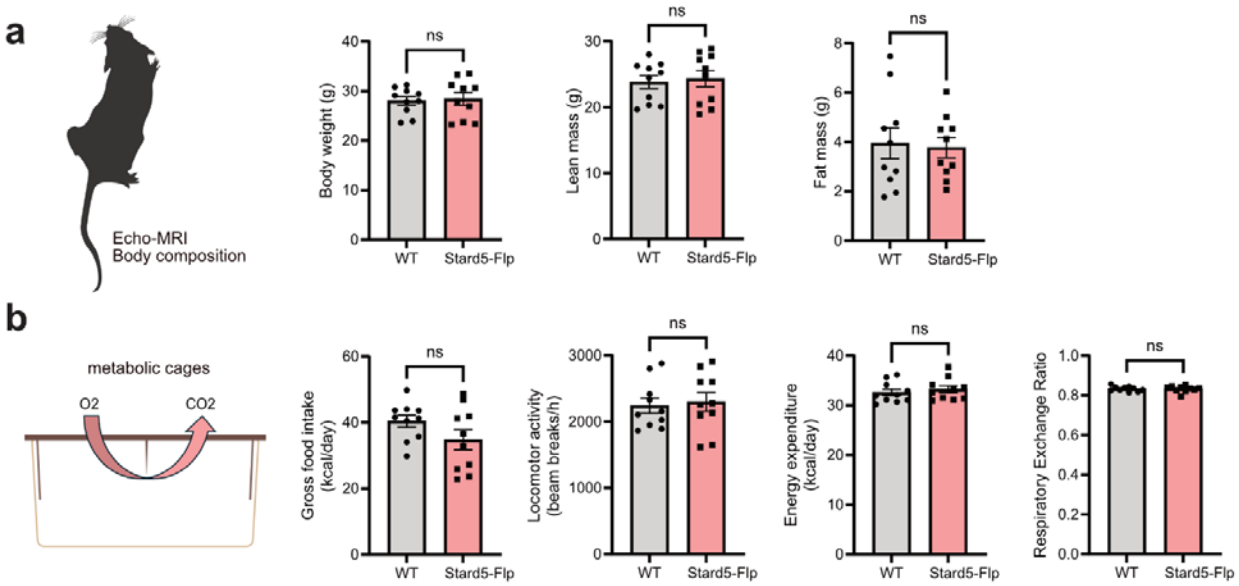

Supplementary Figure S5. The Stard5-Flp transgenic mouse line genetic modification does not show off-target in vivo effects. a. Left: Scheme for the EchoMRI body composition scan and the metabolic cages (data collected across 3 days after 1-3 days habituation). Right: Bar plots showing no significant differences in body weight ($t(18) = 0.2688$, $p = 0.7912$), lean mass ($t(18) = 0.3351$, $p = 0.7415$) or fat mass ($t(18) = 0.2422$, $p = 0.8098$) between Stard-Flp positive and Stard5-Flp negative (wild-type, WT) mice. Paired t-tests, n=10 per group. **b.** Left: Scheme for the metabolic cages/indirect calorimetry. Data collected across 3 days (72 hours) after 1-3 days habituation. Right: Bar plots showing no significant differences in gross food intake ($t(18) = 1.579$, $p = 0.1317$) [this includes metabolizable and non-metabolizable energy], locomotion ($t(18) = 0.3086$, $p = 0.7612$), energy expenditure ($t(18) = 0.6488$, $p = 0.5272$) and respiratory exchange ratio ($t(18) = 0.1100$, $p = 0.9136$) between Stard-Flp positive and Stard5-Flp negative (WT) mice. This indicates a lack of effect of the Stard5-Flp transgene insertion on key in vivo parameters. Paired t-tests, n=10 per group. Data is mean ± SEM. Related to **Figure 6**.

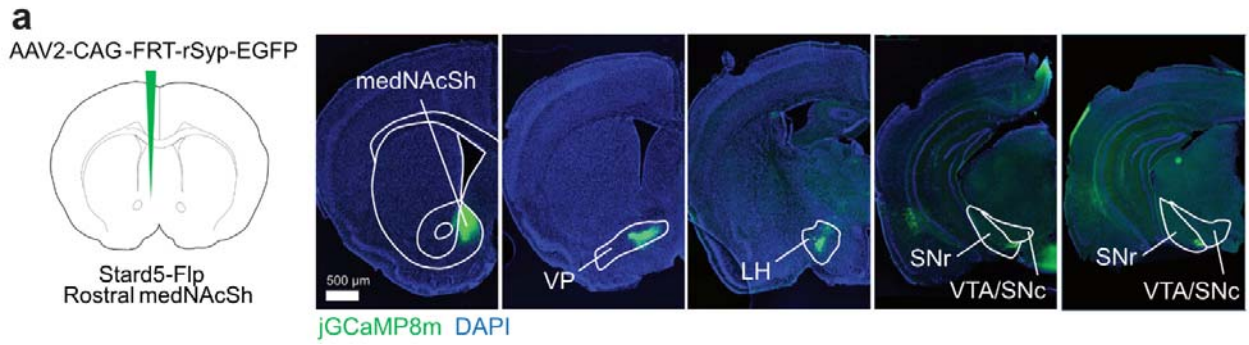

Supplementary Figure S6. The Stard5-Flp mouse line allows to identify projection sites of Stard5 cells. a. Stard5 cells send projections to the canonical projection sites of spiny projection neurons (SPNs) (i.e. D1- and D2-SPNs): the ventral pallidum (VP), lateral hypothalamus (LH) and midbrain. Left: Surgery schematic showing injection of an AAV expressing a flp-dependent fluorophore jGCaMP8m. Right: Representative coronal images showing expression of the fluorophore in the injection site (medNAcSh), as well as in identified projection sites: the VP, LH and midbrain. In the midbrain the strongest expression was in the substantia nigra reticulate (SNr) with some axons in the ventral tegmental area (VTA)/substantia nigra compacta (SNc). Related to **Figure 6**; see also **Supplementary Figure S1**.

SUPPLEMENTARY DATA

Supplementary Data S1. Stard5-2A-Flp0 KI template sequence

Homology arm
RAKR
T2A
FlpO

TATCATCCACAACAAGGAGGCTGAGAGGAGTCCTGGGCACTGAATCTAGAGCAGGAGTAGAAGTGACCACCATGTC
TGGACCACTTCTGCTGGTCATGGCTCTGAGCTAGATGCTTCCATGGTACATATCTAACCCGCATCTGCTATTTCTT
CAGGGATCCCAACAAAACCAACCTGGTCACATTCTTTCAGACAGACCTGAGTGGCTACCTCCCTCAGAGTGTGGTG
GACTCCTTCTTCCCTCGAAGCATGGCTGAGTTCTACCCCAACCTTCAGAAGGCAGTGAGGAAGTTCCATCACAGGG
CAAAGAGGgagggcagaggaagtcttctaacatgcggtgacgtggaggagaatcccggccctatggctcctaagaa
gaagaggaaggtgatgagccagttcgacatcctgtgcaagacccccccaaggtgctggtgcggcagttcgtggag
agattcgagaggcccagcggcgagaagatcgccagctgtgccgccgagctgacctacctgtgctggatgatcaccc
acaacggcaccgccatcaagagggccaccttcatgagctacaacaccatcatcagcaacagcctgagcttcgacat
cgtgaacaagagcctgcagttcaagtacaagacccagaaggccaccatcctggaggccagcctgaagaagctgatc
cccgcctgggagttcaccatcatcccttacaacggccagaagcaccagagcgacatcaccgacatcgtgtccagcc
tgcagctgcagttcgagagcagcgaggaggccgacaagggcaacagccacagcaagaagatgctgaaggccctgct
gtccgagggcgagagcatctgggagatcaccgagaagatcctgaacagcttcgagtacaccagcaggttcaccaag
accaagaccctgtaccagttcctgttcctggccacattcatcaactgcggcaggttcagcgacatcaagaacgtgg
accccaagagcttcaagctggtgcagaacaagtacctgggcgtgatcattcagtgcctggtgaccgagaccaagac
aagcgtgtccaggcacatctactttttcagcgccagaggcaggatcgacccccctggtgtacctggacgagttcctg
aggaacagcgagcccgtgctgaagagagtgaacaggaccggcaacagcagcagcaacaagcaggagtaccagctgc
tgaaggacaacctggtgcgcagctacaacaaggccctgaagaagaacgccccctaccccatcttcgctatcaagaa
cggccctaagagccacatcggcaggcacctgatgaccagctttctgagcatgaagggcctgaccgagctgacaaac
gtggtgggcaactggagcgacaagagggcctccgccgtggccaggaccacctacacccaccagatcaccgccatcc
ccgaccactacttcgccctggtgtccaggtactacgcctacgaccccatcagcaaggagatgatcgccctgaagga
cgagaccaaccccatcgaggagtggcagcacatcgagcagctgaagggcagcgccgagggcagcatcagatacccc
gcctggaacggcatcatcagccaggaggtgctggactacctgagcagctacatcaacaggcggatcTGACAGTCGC
CTATTGGCAGGGATTGCCTATGGTCCTTCAGGAACTCCAGCTGTTGAGCCTCAAAGGACACGGAAGAGCTGCTGAG
GCCTTTTGAGATGCCATAGTTAACAGCAAATCTCAGGGTTCCATTCCAGAGGAGCAGCCCATCCCCCCACACCACC
CTCCGTCCTCTTGGGCTTGGTGTGGAAGGAGCTAACCACTAGCTTGCCGTGGTGCACACATAGGCCTGGCAGGCCA
GGGCAAGTCCCTCTATGGCCACCTGAGAGATGGCTCACGTACTCTTTGATTCCTTGTGGTCC

Supplementary Data S2. Python code in Pynapse for unpredicted reward and unpredicted shock tasks and Optogenetic stimulation during feeding task

Unpredicted Reward Experiment

The experiment is coded in Pynapse (Python-based code in the Synapse software from Tucker Davis Technologies), driving iCON behavioral control units.

Experiment: The session lasts about 30 min. Time-out period of 3 min (180s) at start. Trial duration: 10 s (i.e. lickometer made available). Trial number: 30 times. Inter-trial interval: random intervals, 30 to 50 s. A succesful trial is defined as a trial for which the animal licked the lickometer at least once. For succesful trials, the number of licks is quantified. A lick is defined (within Synapse) as at least 3ms interacting with the lickometer.

Pynapse Code:

```
## Pynapse Source #
import random
import tdt
import numpy

class Always:   #StateID = 0
   def s_Mode_recprev():
      p_Rig.HouseFan.turnOn()
      p_Rig.HouseLight.turnOn()
      p_State.switch(PreTrial)

class PreTrial:    # StateID = 1010
   def s_State_enter():
      p_State.setTimeout(180, Trial1)

class Trial1:    # StateID = 1020
   def s_State_enter():
      p_Rig.RoundLED.turnOff()
      p_Metric.Count.inc()
      p_Metric.FirstLick.write(0)
      random.seed(56)
      p_Metric.ITI_List = []
      for n in range(0,30): #edit to change number of trials or inter-trial intervals (ITI)
         p_Metric.ITI = random.randrange(30,50,1) #edit to change range of ITI
         p_Metric.ITI_List.append(p_Metric.ITI)
      #print(p_Metric.ITI_List)
      print("Succesful trials = ", p_Metric.SuccessfulTrials.read())
      p_State.cancelTimeout()
      if p_Metric.Count.read() <= len(p_Metric.ITI_List) and p_Metric.Trials.read()<=30: #here, 30=total
number of trials (=total number of ITI)
         print("Seconds before next trial = ",p_Metric.ITI_List[p_Metric.Count.read()-1])
         p_State.setTimeout(p_Metric.ITI_List[p_Metric.Count.read()-1],Trial2)
      else:
         p_State.switch(PostTrial)

'''#TIMEOUT ONLY FOR TRAINING! REMOVE FOR ACTUAL EXPERIMENT!!
```

```
    def s_Lick_rise():
        p_Metric.ExtraLicks.inc()
        if p_Metric.ExtraLicks.read()==5: #if more than 5 licks outside the reward window, timeout
initiated
            p_Metric.Timeouts.inc()
            print("lick detected outside reward window; timeout initiated")
            p_State.setTimeout(p_Metric.ITI_List[p_Metric.Count.read()-1]+60, Trial2)
#timeout=60s+whatever the current ITI is
'''
class Trial2:    # StateID = 1030
    def s_State_enter():
        p_Rig.Lickometer.fire()
        p_Metric.Trials.inc()
        print("reward available")
        print("trial number = ", p_Metric.Trials.read())
        p_Metric.ExtraLicks.write(0)
        p_State.setTimeout(10, Trial1)
    def s_Lick_active():
        print("lick")
        p_Metric.Licks.inc() #at end of session, Licks=total number of valid and invalid licks from all reward
windows
        p_Metric.FirstLick.inc()
        if p_Metric.FirstLick.read()==1:
            p_Rig.RoundLED.turnOn()
            p_Metric.SuccessfulTrials.inc()
            print("first lick")
    def s_Lick_fall():
        print("no lick")
    def s_Lick_fail():
        print("invalid lick")
        p_Metric.InvalidLicks.inc() #at end of sesson, InvalidLicks=total number of invalid licks from aa
reward windows

class PostTrial:    # StateID = 1040
    def s_State_enter():
        p_State.setTimeout(180, EndRecording)

class EndRecording:    # StateID = 1050
    def s_State_enter():
        p_Rig.HouseFan.turnOff()
        p_Rig.HouseLight.turnOff()
        syn.setModeStr('Idle')
```

Unpredicted Shock Experiment

The experiment is coded in Pynapse (Python-based code in the Synapse software from Tucker Davis Technologies), driving iCON behavioral control units.

Experiment: Time-out period of 3 min (180s) at start, followed by a 1 s shock delivered 10 times at random intervals between 40 and 80 seconds

Pynapse Code:

```
# Pynapse Source #
import random

class Always:   #StateID = 0
   def s_Mode_recprev():
      p_Rig.HouseFan.turnOn()
      p_Rig.HouseLight.turnOn()
      p_State.switch(PreTrial)

class PreTrial:    # StateID = 1010
   def s_State_enter():
      p_State.setTimeout(180, InterTrialInterval)

class InterTrialInterval:    # StateID = 1020
   def s_State_enter():
      p_Metric.Count.inc()
      random.seed(98)
      iti_list = []
      for n in range(0,10):
         iti=random.randrange(40,80, 1)
         iti_list.append(iti)
      #print(iti_list)
      p_State.cancelTimeout()
      if p_Metric.Count.read() <= len(iti_list) and p_Metric.Shocks.read()<=10:
         print("seconds before next shock = ", iti_list[p_Metric.Count.read()-1])
         p_State.setTimeout(iti_list[p_Metric.Count.read()-1],Shock)
      else:
         p_State.switch(PostTrial)

class Shock:    # StateID = 1030
   def s_State_enter():
      p_Rig.GridShock.fire()
      print("shock given; trial number = ",p_Metric.Count.read())
      p_Metric.Shocks.inc()
      p_State.switch(InterTrialInterval)

class PostTrial:    # StateID = 1040
   def s_State_enter():
      p_State.setTimeout(180, EndRecording)

class EndRecording:    # StateID = 1050
   def s_State_enter():
      p_Rig.HouseFan.turnOff()
```

```
p_Rig.HouseLight.turnOff()
syn.setModeStr('Idle')
```

Optogenetic stimulation during reward task

Reward is available at all times. Optogenetic stimulation, triggered by TDT (5 minutes, 20 Hz)

```
## Pynapse Source #
#this code has 5 blocks:  trial 1 opto STIM,  trial 2 NO stim, trial 1 opto STIM,  trial 2 NO stim,  trial 5 OPTO STIM
#each block is 5 min long

import random
import tdt
import numpy

class Always:   #StateID = 0
   def s_Mode_recprev():
      p_Rig.HouseFan.turnOn()
      p_Rig.HouseLight.turnOn()

      p_Timer.MyTimer.turnOn()
      p_State.switch(PreTrial)
class PreTrial:    # StateID = 1010
   def s_State_enter():
      print("Baseline 2 s")
      p_Metric.TrialCounter.write(0)  # Initialize a counter to track the number of trials
      p_State.setTimeout(2, Trial1)

class Trial1:    # StateID = 1030
   def s_State_enter():
      p_Output.StartLaser.fire()  # Turn on the laser 20 Hz stim continous
      p_Metric.Trials.inc()
      print("Trial 1: OPTO stimulation, trial Nr.", p_Metric.Trials.read())
      p_State.setTimeout(300, SwitchTrial)  # After 5 minutes (300 seconds), switch to next trial

   def s_Lick_active():
      print("lick")
      p_Metric.Licks.inc()



class Trial2:    # StateID = 1031
   def s_State_enter():

      p_Metric.Trials.inc()
      print("Trial 2: NO opto stim 5 min, trial Nr. ", p_Metric.Trials.read())
      p_State.setTimeout(300, SwitchTrial)  # After 5 minutes (300 seconds), switch to next trial

   def s_Lick_active():
      print("lick")
      p_Metric.Licks.inc()


class SwitchTrial:   # StateID = 1040
   def s_State_enter():
      current_trial = p_Metric.TrialCounter.read()
      if current_trial < 4:  # Check if there are more trials to run
         if current_trial % 2 == 0:  # If the trial count is even, switch to Trial 2
            p_State.switch(Trial2)
         else:  # If the trial count is odd, switch to Trial 1 (opto stim)
```

```
            p_State.switch(Trial1)
        p_Metric.TrialCounter.inc()
    else:
        p_State.switch(PostTrial)  # After 5 trials (Trial 1 Trial 2 Trial 1 Trial 2 Trial 1), end the session

class PostTrial:    # StateID = 1050
    def s_State_enter():
        #p_Rig.Speaker2.fire()
        print("POST TRIAL: 5 seconds left!!!!")
        p_State.setTimeout(5, EndRecording)

class EndRecording:    # StateID = 1060
    def s_State_enter():
        p_Rig.HouseFan.turnOff()
        p_Rig.HouseLight.turnOff()
        syn.setModeStr('Idle')
```

Supplementary Data S3. Source Data (Separate Excel file)